CCN Activity, Closure and Droplet Growth Kinetics of Houston Aerosol During the Gulf of Mexico Atmospheric Composition and Climate Study (GoMACCS)

Sara Lance and Athanasios Nenes*, Georgia Institute of Technology; Claudio Mazzoleni, Michigan Technological University; Manvendra Dubey, Los Alamos National Laboratory; Harmony Gates, Varuntida Varutbangkul, Tracey A. Rissman, Shane M. Murphy, Armin Sorooshian, Richard C. Flagan and John H. Seinfeld, California Institute of Technology; Graham Feingold, National Oceanic and Atmospheric Administration; Haflidi H. Jonsson, Naval Postgraduate School

For Publication in
Journal of Geophysical Research – Atmospheres
TexAQS/GoMACCS special issue

* Corresponding author

ABSTRACT

In-situ Cloud Condensation Nuclei (CCN) measurements were obtained in the boundary layer over Houston, TX during the 2006 Gulf of Mexico Atmospheric Composition and Climate Study (GoMACCS) campaign onboard the CIRPAS Twin Otter. Polluted air masses in and out of cloudy regions were sampled for a total of 22 flights, with CCN measurements obtained for 17 of these flights. In this paper, we focus on CCN closure during two flights, within and downwind of the Houston regional plume and over the Houston Ship Channel. During both flights, air was sampled with particle concentrations exceeding 25,000 cm^{-3} and CCN concentrations exceeding 10,000 cm^{-3}. CCN closure was evaluated by comparing measured CCN concentrations with those predicted on the basis of measured aerosol size distributions and Aerosol Mass Spectrometer particle composition. Different assumptions concerning the internally-mixed chemical composition result in average CCN overprediction ranging from 3% to 36% (based on a linear fit). It is hypothesized that the externally-mixed fraction of the aerosol contributes much of the CCN closure scatter, while the internally-mixed fraction largely controls the overprediction bias. Finally, based on the droplet sizes of activated CCN, organics do not seem to impact, on average, the CCN activation kinetics.

1. Introduction

In addition to human health and direct climate radiative forcing implications, aerosols play an important role in the formation of clouds, as they provide the sites upon which cloud droplets form. Higher aerosol concentrations generally lead to a greater number of cloud droplets, but not all particles are equally efficient CCN. Each particle requires exposure to a threshold water vapor concentration, termed "critical supersaturation", before acting as a cloud condensation nucleus (CCN) and spontaneously activating into a cloud droplet. The complexity of aerosol-cloud interactions, and, the strong impact of clouds on the planetary radiative budget leads to an "aerosol indirect climate effect" that constitutes the largest source of uncertainty in anthopogenic climate change predictions [IPCC, 2007].

The conditions under which a particle can act as a CCN depend strongly on particle size [e.g., Seinfeld and Pandis, 2006] although particle composition also plays an important role. The latter effects are a challenge for predictive models, as they require simulating the evolution of the aerosol population as it ages and interacts with fresh emissions. Dusek et al [2006] suggest that the aerosol composition has only a minor effect on CCN concentrations, with variability in the size distribution alone accounting for 84-96% of the variability in CCN concentrations. Wang [2007] showed that cloud albedo is insensitive to particle composition. Others however have found that the mass fraction of one type of chemical compounds, known as Hydrocarbon-like Organic Aerosol (HOA), can explain up to 40% of the CCN concentration variability [Quinn et al, 2008]. Furutani et al [2008] also found that changes in aerosol composition from aging processes can have an important effect on CCN activity.

64 To predict CCN concentrations for a given particle size distribution, simplifying
65 assumptions are typically made for the chemical composition of the aerosol population;
66 this is the case even when composition measurements are available, since no
67 measurement technique is capable of quantifying the full array of compounds present in
68 ambient aerosol [Saxena and Hildemann, 1996]. Solubility, density, molecular weight,
69 and surfactant properties all affect CCN activity [Saxena and Hildemann, 1996], as do
70 interactions between the organic and inorganic aerosol constituents [Shulman et al, 1996;
71 Dinar et al, 2008]. Most often, Aerodyne Aerosol Mass Spectrometer (AMS)
72 measurements are used to constrain the chemical properties of the soluble inorganic
73 fraction of ambient aerosol (nitrate, sulfate and ammonium ions) for CCN studies [e.g.,
74 Ervens et al, 2007; Medina et al, 2007]. However, AMS measurements are unable to
75 provide the refractory composition (e.g. soot) or complete speciation of the organic
76 fraction. Numerous simple approaches have been proposed, based on activation spectra
77 or hygroscopic uptake properties of carbonaceous aerosol, to characterize the impact of
78 organics on water activity and CCN activity [e.g., Petters and Kreidenweis, 2007; Vestin
79 et al, 2007; Padró et al., 2007]. Although very useful for parameterizing ambient data
80 measurements, these methods are often applied with the assumption that the organic
81 fraction is water-soluble and does not affect surface tension behavior, both of which
82 result in inferred hygroscopicity that may not reflect the properties of the water-soluble
83 carbonaceous fraction of the aerosol [e.g., Englehart et al., 2008; Asa-Awuku et al,
84 2008b].

85 Apart from the diversity of organic compounds present in ambient aerosol,
86 another important source of uncertainty in predicting CCN concentrations is the mixing-

state of the aerosol population, especially close to emission sources. Modeling studies often assume that particles are internally-mixed (i.e., all particles of a given size have the same composition); in reality, the aerosol is often an external-mixture, and chemical composition varies amongst particles of the same size. Since the soluble (typically inorganic) components dominate the water-uptake properties of the aerosol, the existence of externally-mixed hydrophobic particles can have an important impact on CCN number.

CCN closure studies have been performed over the last decade to evaluate the predictive understanding of the aerosol-CCN link [e.g., VanReken et al, 2003; Chang et al, 2007; Cantrell, 2001; Medina et al, 2007; Broekhuizen et al, 2006; Ervens et al, 2007, and references therein]. These studies use measurements of the aerosol size distribution and chemical composition to predict the number of CCN for a given supersaturation; direct in-situ observations of CCN (obtained by exposing the ambient particles to a controlled water vapor supersaturation) are then compared against these predictions. Most often, CCN concentration is overpredicted on average by less than ~30%; the variability however is often much larger and difficult to account for.

The current work focuses on CCN measurements taken onboard the Center for Interdisciplinary Remotely-Piloted Aircraft Studies (CIRPAS, http://www.cirpas.org) Twin Otter during the Gulf of Mexico Atmospheric Composition and Climate Study (GoMACCS) field campaign in Houston, TX from August 25-September 15, 2006 (http://esrl.noaa.gov/csd/2006/). Owing to a combination of motor vehicle traffic, close proximity to large petrochemical refineries, chemical plants, waste treatment, coal-fired power plants, and heavy industrial shipping via the Houston Ship Channel, measured

aerosol concentrations often exceeded 10,000 cm^{-3}. Houston, with its diverse mixture of local industrial sources in combination with the local marine and biogenic emissions, is an especially challenging area in which to predict the effect of aerosols on clouds. We study the ability to predict CCN concentrations in a heavily polluted environment, in which organic concentrations are often high, and explore the role of the particle chemical composition in the variability and biases of our CCN predictions. This study is complementary to the study of Quinn et al [2008], which took place over the same time period onboard the NOAA ship *Ronald H. Brown*, and, the study of Asa-Awuku et al [in review], which took place onboard the NOAA WP-3D airborne platform.

2. Dataset Description

2.1 Overview of Flights

Figure 1a shows the flight tracks for the Twin Otter Research Flights (RF) analyzed, each of which occurred during daylight hours. A total of 22 flights were carried out, during which airmasses were sampled in the vicinity of powerplants (RF1-3, 9, 13, 14, 17, 19), the Houston Ship Channel (RF 4, 11), Downtown Houston (RF 11, 13, 21, 22) and its surrounding areas. Supersaturation in the measurements varied from 0.3 to 1.0%, and CCN concentrations, from 200 to 15,000 cm^{-3}. Table 1 shows a summary of the flights, the major sources of pollution, and the dominant wind direction. Lu et al [2008] describe the complete instrument payload on the Twin Otter during GoMACCS.

2.2 CCNc Measurements

CCN concentrations were measured using a Droplet Measurement Technologies continuous flow streamwise thermal gradient CCN counter (CCNc; Roberts and Nenes, 2005; Lance et al., 2006) at 1 Hz time-resolution. CCN were sampled through a manifold from which all other in-situ aerosol observations were taken (except for the particle size distribution measurements, which will be discussed later). The common sampling manifold was located downstream of a ball valve set to sample either from the main inlet (Figure 1b) or downstream of a Counterflow Virtual Impactor [Noone et al, 1988; Ogren et al, 1992], which selectively sampled droplets and large particles with diameters exceeding ~5 μm, and was switched on during constant altitude legs in-cloud. CCN measurements were obtained for the aerosol outside of cloud, and, for the cloud droplet residuals.

The supersaturation within the CCNc is controlled by the sample and sheath flow rates, column pressure, inlet temperature, and the temperature difference between the bottom and top of the column. The uncertainty for each of these operating parameters is summarized in Table 2. The CCNc was operated throughout the campaign with a set flow rate of ~1 L min^{-1}, consisting of sample and sheath flows with average rates of 0.092 and 0.909 L min^{-1}, respectively. The careful design of the Twin Otter main inlet (which decelerates the air flow by a factor of ten before it enters the sampling manifold) dampens most pressure oscillations; changes in attack angle of the aircraft still generate high frequency (small amplitude) pressure fluctuations which are magnified by the active flow control in the CCNc and create flow oscillations in the growth chamber. To address this, a flow restriction upstream of the CCNc was used in most flights to dampen residual pressure fluctuations in the main sampling inlet. Without a flow restrictor (RF4), the

sheath flow rate standard deviation increased by a factor of 4 (see Table 2). For RF7, the flow restrictor was replaced with a 0.33m long, 1.9cm diameter dead volume (with an added delay time of 4.4s), which resulted in flow rate fluctuations comparable to leaving the flow restrictor off.

Hegg et al. (2005) report that the transmission efficiency of the Twin Otter main inlet is close to 100% for particle diameters less than 3.5 μm. Similarly, particle losses through the flow restrictor have been found to be negligible for submicron particles in the range of pressures and flow rates experienced during flight. Since nearly all CCN are below 300 nm, number losses for CCN in both the main inlet and in the flow restrictor upstream of the CCNc are negligible.

In addition to pressure fluctuations, the CCNc is sensitive to low-frequency pressure changes during ascents and descents owing to the finite time required for the development of the temperature and supersaturation profiles within the instrument; this issue was addressed by maintaining the pressure at the inlet of the CCNc at ~700 mb using a DMT Inlet Pressure Controller (http://www.dropletmeasurement.com). It consists of a vacuum pump with active flow control pulling downstream of the flow restrictor and in parallel to the CCNc. The pressure controller flow was set to maintain the pressure at the inlet of the CCNc to a constant value. The pressure controller was operated upstream of the CCNc for all but RF4, RF5, RF6, RF7 and RF9.

The reduced pressure in the CCNc expands the sample volume and decreases the CCN concentration, requiring correction of the measured concentrations back to ambient concentrations, according to the ideal gas law:

$$[CCN]_{amb} = [CCN]_{meas}\left(\frac{P_{amb}}{P_{CCN}}\right) \quad (1)$$

where $[CCN]_{amb}$ and $[CCN]_{meas}$ are the ambient and measured CCN concentrations, and P_{amb} and P_{CCN} are the ambient and CCNc pressures, respectively. As the inlet pressure controller was not installed until midway through the mission, supersaturation in the CCNc during RF4, RF5, RF6, RF7 and RF9 drifted with the ambient pressure. For these flights, data collected during altitude changes are not considered.

In addition to pressure changes, the drifting temperature of the CCNc inside the fuselage of the Twin Otter can cause changes in the CCNc supersaturation. The CCNc control software sets the column temperature at the top (T1) to a constant offset above ambient temperature for the thermal electric coolers to operate efficiently. The temperature setpoints at the middle and bottom of the column (T2 and T3, respectively) are adjusted accordingly, to maintain a constant setpoint temperature difference (T3-T1). For this study, the ambient temperature is the uncontrolled temperature within the unpressurized cabin of the aircraft, which heats up from the nearby pumps in an enclosed space and cools off as the aircraft ascends to higher altitudes. The T1 setpoint does not continuously follow ambient temperature, rather only when the ambient temperature exceeds 1°C difference from T1. Thus, the temperature setpoint increments in step changes as the ambient temperature drifts, which occasionally causes slight but abrupt changes in supersaturation.

Uncertainty in the temperature difference between the bottom and top of the CCNc column translates directly to uncertainty in the CCNc supersaturation. The temperature uncertainty was significantly higher in the early flights compared to later

199 flights, as shown in Table 2. Starting with the flight on September 1, 2006 (RF11), a new
200 AC/DC power supply was installed, which significantly reduced the temperature
201 fluctuations recorded by the thermisters in the CCNc, bringing the temperature variability
202 down to levels observed in laboratory experiments and ground-based studies. The high-
203 frequency variability in recorded temperatures in the earlier flights cannot be real (as the
204 thermal resistance in the flow column does not permit such high-frequency fluctuations)
205 and is likely a result of electronic noise; nevertheless, we treat the measured temperature
206 uncertainty as true, leading to significantly higher supersaturation uncertainty (Table 2).

207 For several of the research flights (RF7, RF11, RF16 and RF17) the CCNc was
208 operated at multiple supersaturations by periodically making step-changes in the vertical
209 (streamwise) temperature gradient. The temperature gradient cycling was automated and
210 was not, therefore, purposely aligned with the sampling of plumes. For flights after
211 August 31, the supersaturation was maintained at $0.5 \pm 0.03\%$ (one standard deviation).

212 The CCNc supersaturation was calibrated throughout the mission at various
213 pressures, flow rates, and temperature gradients using laboratory-generated ammonium
214 sulfate particles (following the SMCA procedure of Nenes and Medina, in review; Asa-
215 Awuku et al., 2008b). These calibrations were then used to determine the supersaturation
216 at different operating conditions during flight, interpolating between the calibrated
217 supersaturations when required using the thermal efficiency and supersaturation
218 parameterizations from Lance et al [2006]. The slope and intercept of the supersaturation
219 versus ΔT curve were accounted for in the calculations of thermal resistance, assuming a
220 van't Hoff factor of 2.5 and spherical shape for the dry ammonium sulfate calibration
221 aerosol [Rose et al, 2008; Zelenyuk et al, 2006].

Figure 2 shows a summary of the operating conditions and the variability therein for four representative flights (RF7, RF9, RF11, RF19). The uncertainty in their operating conditions can be classified in four different categories. Flights classified in Categories 1 and 3 (corresponding to RF7 and RF11 in Figure 2) had a changing supersaturation setpoint (three different values changing every 5 min throughout the flight). The uncertainty in supersaturation at each setpoint, however, is much higher for Category 1 flights than for Category 3 flights due to a greater uncertainty in the sheath flow rate and/or column temperature gradient. Flights designated as Category 1 also had a drifting pressure in the CCNc (except for RF7, where the entire flight was at constant altitude) causing shifts in supersaturation, while Category 3 flights made use of the inlet pressure controller. The supersaturations for the Category 3 flight shown (RF11) remain consistent throughout, even as the ambient pressure changes (except when pressure drops the pressure box control setting of 700 mbar). Even with the pressure control box, minor supersaturation deviations still exist owing to changes in ambient temperature. Category 2 and 4 (represented by RF9 and RF19 in Figure 2) were set to a single supersaturation, but with pressure changes, and larger uncertainty in flow and temperature uncertainty in the former. Because the supersaturation was set to a constant value for the Category 2 and 4 flights, it is easier to see the effect of the abrupt change in the temperature setpoint as the ambient temperature changed inside the cabin of the aircraft.

Although the variance of the calculated instrument supersaturation is low, Rose et al. [2008] suggest that the relative supersaturation uncertainty (at low supersaturations) can be as high as 10% due to uncertainties in the parameters used to calibrate the instrument, such as water activity and nonspherical particle shape. We assume 10% as an

upper limit of supersaturation uncertainty for Category 3 and 4 flights, and we assume an uncertainty in supersaturation of 20% for Category 1 and 2 flights. Instrument supersaturation uncertainty translates to uncertainty in the predicted CCN concentrations; for the levels cited here it could be important depending on the steepness of the CCN spectrum (which is a convolution of aerosol size distribution, composition and mixing state) at the supersaturation of interest. Although not straightforward, the sensitivity of CCN concentration to supersaturation uncertainty can be evaluated from the observed particle size distributions, given assumptions about the particle composition (Section 2.4).

2.3 Measurements used for CCN closure

Measurements used for CCN closure calculations (in addition to CCN concentrations) are dry particle size distributions (with relative humidity at 21% ± 5 %, during all flights) measured by the Dual Automated Classified Aerosol Detector (DACAD [Wang et al., 2003]), and, the aerosol chemical composition measured by an Aerodyne compact time of flight aerosol mass spectrometer (C-ToF-AMS [Drewnick et al, 2005; Sorooshian et al, 2008]). The CCNc and C-ToF-AMS were positioned on the same aerosol sampling manifold, which was switched between "counterflow virtual impactor in-cloud", and, "main inlet out-of-cloud" modes. Since the DACAD sampled continuously from the main inlet, mobility size distribution measurements of cloud droplet residuals were not available, and therefore CCN closure cannot be evaluated for cloud droplet residuals. In computing the size distribution, we assume that particles measured in the DACAD are spherical, which is typically valid in a humid environment

(even when the aerosol is dried appreciably), due to depression of the efflorouescence point by the organic compounds present in the particle [Salcedo, 2006; Chan et al, 2008].

An important temporal limitation is associated with the measurement of aerosol size distribution (73 seconds). For each scan, the average number concentration of CCN and supersaturation within the CCNc is computed. This dataset is then filtered by disregarding 73 s-segments of data when the CCNc instrument supersaturation varies by 20% or more (from column temperature changes or pressure fluctuations during ascents/descents). To disregard aliasing biases from sampling smaller plumes that are below the temporal resolution of the DACAD, we filter out points for which the standard deviation of CCN exceeds 25% of the average CCN concentration. We further filter out data points when the average Condensation Nuclei (CN) concentrations differ by more than 50% from the total particle concentrations integrated from the measured DACAD size distribution.

For the CCN closure analysis, we use bulk chemical composition from the C-ToF-AMS measurements, unless specified otherwise. Size-resolved AMS measurements have been used for several ground- and ship-based CCN closure studies [e.g., Medina et al. 2007; Ervens, et al. 2007; Quinn et al. 2008], where the airmass passes at a rate of 1 to 10 m s^{-1}. In airborne CCN closure studies, the airspeed is 10 to 100 times greater and airmass composition changes rapidly, requiring higher sensitivity and time-resolution for the size-resolved composition measurements. While size-resolved measurements can be obtained rapidly in high concentration plumes [e.g. Murphy et al, 2009; Sorooshian et al, 2008], the loadings during many portions of the flights in this study were too low to obtain size-resolved composition in reasonably short time frames. As a result, size-

291 resolved data was not used for CCN closure in this paper. However, the effect of size-
292 resolved composition measurements is shown for specific cases where the signal-to-noise
293 ratio for both the sulfate and organic size distributions is high.

294 A Droplet Measurement Technologies integrated Photoacoustic and nephelometer
295 Aerosol Spectrometer (PAS) was also operated onboard the CIRPAS Twin Otter. The
296 PAS measures aerosol absorption and ~5^{o}-175^{o} integrated scattering, using a laser
297 radiation source, and an acoustic resonator coupled with a microphone to detect the
298 photoacoustic signal from absorption. A Lambertian diffuser, mounted at the center of the
299 acoustic resonator, is used to measure the light scattered by the aerosol. The standard
300 laser installed by the manufacturer is a 781 nm solid state laser which failed under the
301 high temperatures experienced in the aircraft cabin during some of the flights (a
302 replacement 870 nm laser was then used for the rest of the campaign). The PAS collects
303 data at a sampling rate of ~0.71 Hz. Zero air (cleaned of particles by means of a HEPA
304 filter) data are automatically collected every ~4.7 minutes to correct for background
305 drifts. A thorough calibration of the PAS (with the 870 nm laser) was carried out at the
306 end of the campaign in the laboratory using various concentrations of strongly and
307 weakly absorbing particles. Altogether, the calibration procedure, instrumental noise and
308 high frequency changes in the background signals introduce an estimated 20-30%
309 uncertainty in the absorption measurements discussed here. A PAS prototype, developed
310 at the Desert Research Institute, Reno, NV, has been extensively tested and successfully
311 deployed in past field campaigns [Arnott, 1998; Arnott, 1999; Moosmüller, 1998; Arnott,
312 2006]. PAS observations are shown for one flight (using the 870 nm laser) to infer the
313 impact of soot on CCN concentrations.

314

315 *2.4 Prediction of CCN concentrations*

316 To predict CCN concentrations from the measured size distribution (assuming
317 that all particles have an internally-mixed composition), we first determine the diameter
318 of the smallest CCN-active particle (d_{50}; where "50" signifies that a dry particle with this
319 size has a 50% probability of activating into a cloud droplet) given the assumptions about
320 internally-mixed particle chemistry, using the following thermodynamic relationship
321 [Seinfeld and Pandis, 2006]:

322

323 $$d_{50} = \left[\frac{27}{4} \left(\ln\left(\frac{S}{100} + 1 \right) \right)^2 \left(\frac{\rho_w TR}{4 M_w \sigma} \right)^3 \frac{\rho_s M_w \varepsilon_s \upsilon}{M_s \rho_w} \right]^{-1/3} \quad (2)$$

324

325 where S is the average instrument supersaturation (in %), T is the mean temperature
326 within the CCNc column, R is the ideal gas constant, σ is the droplet surface tension at
327 the point of activation, ρ is the density and M is molecular weight of the solute
328 (subscript s) and of water (subscript w), and ε_s and υ are the solute volume fraction
329 and effective van't Hoff factor, respectively. Unless specified otherwise, the surface
330 tension used in Equation 2 to predict CCN concentrations is 69.9 mN m^{-1}, which is the
331 surface tension of pure water at the average temperature of the observations. CCN
332 predictions are calculated by summing all particles with diameters above d_{50}, accounting
333 for fractional activation of the DACAD size bin containing d_{50}.

334 For the flights where chemical composition information is used, we assume that
335 the measured species are internally-mixed. Furthermore, since the solubility of organics,

their surfactant properties and mixing state are unknown, they are first treated as insoluble and non-surfactant (the effect of these assumptions on CCN closure is addressed with appropriate sensitivity studies). The organic volume fraction (ε_{org}) is then computed as:

$$\varepsilon_{org} = (1 - \varepsilon_s) = \frac{m_{org} / \rho_{org}}{m_{org} / \rho_{org} + m_{AS} / \rho_{AS}} \quad (3)$$

where m_{org} and m_{AS} are the mass loadings of organics and ammonium sulfate (the sum of ammonium and sulfate ions) obtained from the C-ToF-AMS, respectively, ρ_{AS} is the density of ammonium sulfate (1.76 g cm^{-3}; Hinds, 1999) and ρ_{org} is an average density of organics, assumed to be 1.4 g cm^{-3}. The density of organics may range from 1.4 g cm^{-3} to more than 1.6 g cm^{-3} [Dinar et al, 2006]; we use the lower end of the organic density range to simulate the largest effect expected from internally-mixed organics, as further explained in the following paragraph. When not including the bulk aerosol composition, we assume as a zero-order approximation that particles are composed of ammonium sulfate (ε_s = 1.0 in Equation 2). Following the guidance of Rose et al [2008], υ for ammonium sulfate (whether pure or internally-mixed with organics) is set to 2.5.

The two compositional assumptions presented above (pure ammonium sulfate vs. internally-mixed insoluble organic) represent limiting states of aerosol hygroscopicity. Ammonium sulfate is one of the most CCN-active and abundant compounds found in accumulation mode aerosol; assuming that the particles are composed purely of ammonium sulfate will thus tend to overestimate their CCN activity. Conversely, assuming organics are insoluble neglects their potentially important impacts on droplet

activation, thereby leading to a tendency for underpredicting CCN number. In reality, we expect that the hygroscopicity of ambient particles lies somewhere between these two extremes. There are many other details about the aerosol composition that may affect the CCN closure (such as surfactant components, externally-mixed particles, and size-varying composition), which are insufficiently constrained by the observations. We therefore first apply these two common assumptions to the whole dataset to evaluate how well CCN closure can be attained. We then evaluate for specific cases the impact of more detailed composition information on CCN prediction accuracy.

The uncertainty in predicted CCN concentration is influenced by uncertainties in the instrument supersaturation, particle size distribution and chemical composition. Assuming an internally-mixed composition that is invariant with particle size, an estimate of CCN concentration sensitivity to supersaturation uncertainty can be obtained. For a period of very poor closure at ~16:15 UTC on RF22, a 10% reduction of the instrument supersaturation causes a slight increase in d_{50} (from 46.4 nm to 53.0 nm), which decreases the predicted CCN concentrations from 1630 cm^{-3} to 1470 cm^{-3}. Given that the measured CCN concentrations are only 580 cm^{-3} during this time period, the uncertainty in predicted CCN concentrations clearly cannot explain the poor closure for this example.

3. Results

3.1 Summary of CCN observations

Table 1 summarizes the range of CCN concentration and supersaturation for all research flights during which the CCNc was operating. Figure 3a shows the profile of 1Hz CCN data from the entire GoMACCS campaign as a function of ambient pressure,

and colored by date. For many of the flights, CCN concentrations exceeded 10,000 cm^{-3} (for a range of supersaturations, from 0.3 – 1.0 %). On separate days, the CCN concentrations exceeded 20,000 cm^{-3} (again, for a range of supersaturations, as low as 0.3%). Figure 3b shows the frequency distribution of CCN concentrations with different supersaturation ranges over the entire GoMACCS campaign. The solid line indicates the sum of the shaded regions, which is the total frequency distribution of CCN.

3.2 CCN Closure

We first evaluate the extent to which CCN closure can be achieved using the measured size distribution and the assumption of pure ammonium sulfate particles. Figure 4a shows a summary of this simplified CCN closure colored by flight, for all the flights shown in Figure 1a. The gray lines indicate over- and under- prediction by factors of two, three and four, respectively. Despite the very simple composition assumption, predictions are nearly always within a factor of two greater than the measurements. Figure 4b shows that the simplified CCN closure error is not correlated with supersaturation, but rather with particle concentration. The overprediction (~36%) is constant for CCN concentrations ranging from 1,000 to 10,000 cm^{-3}. At lower CCN concentrations (suggestive of a cleaner airmass), the bias is lower. At the highest concentrations (above 10,000 cm^{-3}), the overprediction bias decreases again. Since there is no clear dependence of the CCN overprediction on instrument supersaturation and CCN concentration, water vapor depletion in the CCNc is unlikely the cause for the CCN overprediction observed (laboratory experiments further support this, as they have shown that water vapor depletion does not reduce the maximum supersaturation in the CCNc for

403 CCN concentrations up to at least 10,000 cm^{-3}). Instead, the composition of the aerosol
404 population is expected to play a role.
405
406 *3.3 CCN Closure with Chemical Analysis*
407 Figure 5 shows the CCN closure for all flights to which bulk aerosol chemical
408 composition from C-ToF-AMS data is applied. In both Figure 5a and 5b, the colored
409 data points correspond to CCN closure calculations assuming that organics are internally-
410 mixed with sulfate for all particles. Figure 5a shows the CCN closure colored by flight
411 and Figure 5b is colored by the instrument supersaturation. The black "+" symbols show
412 the CCN closure assuming pure ammonium sulfate aerosol. A linear regression of
413 predicted versus observed CCN concentrations, when forced through the origin, gives a
414 slope of 1.365 ± 0.007 for the assumption of ammonium sulfate particles (with an R^2
415 value of 0.906) and a slope of 1.026 ± 0.006 for the assumption of internally-mixed,
416 insoluble organics (with an R^2 value of 0.907). The linear regression was forced through
417 the origin because a statistically significant linear offset was not supported by the data.
418 In addition to the linear regression, we also calculate the average CCN overprediction
419 bias using a "ratio method" by fitting a Gaussian curve to histograms of the ratio of
420 predicted to measured CCN concentrations; this representation of the CCN closure
421 prevents the higher CCN concentration observations from controlling the fit. The result
422 is a more modest improvement in CCN closure from the inclusion of bulk chemical
423 information (with a decrease in the CCN overprediction bias from 34% to 20% using the
424 ratio method, as opposed to a decrease from 36% to 3% using the linear fit).
425 Furthermore, using the ratio method, the standard deviation decreases slightly from 24%

426 to 19% when including the bulk chemical information (which is a more significant
427 change than that of the linear regression coefficients). Overall, these results are
428 consistent with studies published to date [e.g., Medina et al., 2007; Chang et al. 2007;
429 Wang et al., 2008; Ervens et al, 2007], which show that CCN concentrations can be more
430 accurately predicted assuming that the measured organics are insoluble.

431 Organics can also lower the surface tension of deliquesced CCN, facilitating
432 activation (potentially making the particles even more CCN-active than ammonium
433 sulfate; Asa-Awuku et al, 2008a). Figure 5a presents the impact of reducing surface
434 tension by 15 mN m^{-1} on CCN closure (grey "+" symbols), using the same composition
435 information as the colored data points. This degree of surface tension reduction is typical
436 for organic-rich ambient particles [e.g., Facchini et al, 2000; Decesari et al, 2005; Mircea
437 et al, 2005; Asa-Awuku et al, 2008a]. The modest surface tension depression may
438 reconcile the CCN underprediction bias, even for cases where the aerosol is mostly
439 composed of ammonium sulfate.

440 Although simply adding the assumed internally-mixed organic fraction to the
441 CCN closure analysis reduces the overprediction bias, it cannot be established if the
442 improved CCN closure occurs for the right reasons. It may be hypothesized that the CCN
443 overprediction bias is controlled by the internally-mixed aerosol composition (as
444 measured by the C-ToF-AMS), whereas the variability in the CCN closure is governed by
445 the externally-mixed hydrophobic fraction (assuming that a significant fraction of the
446 externally-mixed hydrophobic aerosol mass is undetected by the C-ToF-AMS, such as
447 soot and dust); this would be consistent with the reduced bias resulting from the
448 internally-mixed assumption without a large reduction in the variability (since the

449 mixing-state is unknown). Without particle-by-particle information or measurements of
450 the aerosol mixing-state, it is not possible to verify this hypothesis. Hygroscopicity
451 measurements (especially with high temporal resolution, e.g. the DASH [Sorooshian et
452 al, 2008b]), or single-particle mass spectra measurements in the size range 40-200nm,
453 may be needed to adequately address the affect of aerosol composition on CCN closure.
454 In the following sections, we examine specific flights and the CCN closure in
455 relation to specific aerosol sources, in an attempt to evaluate the chemical factors
456 influencing the observed CCN concentrations.
457
458 *3.4 Research Flight 7 (Aug 28, 2006)*
459 During RF7, backtrajectories computed with the Flexpart model
460 (http://zardoz.nilu.no/~andreas/TEXAQS/) suggest the wind blew consistently out of the
461 Gulf of Mexico and then curved towards the northeast over the city of Houston. The
462 consistent meteorology provided an opportunity to examine the evolution of emissions
463 from specific chemical plants and refineries along the Houston Ship Channel as the
464 emissions traveled downwind. Figure 6a shows the flight track for RF7, colored by the
465 time of day, first starting at Ellington Field southeast of downtown Houston, followed by
466 transects of the Houston plume downwind, then followed by approaches toward and
467 away from specific point sources previously identified. The plumes identified by particle
468 concentrations in excess of 10,000 cm^{-3} (colored in grey) appear to be correlated with
469 specific point sources identified in the 2004 EPA NO_x emission inventory. Figure 6b
470 presents the flight track colored by the organic volume fraction (calculated from Equation
471 3), which ranges between 0 and 0.3 for this flight, with the higher values at roughly the

same locations as those of elevated particle concentrations. The maps (Figures 6a,b) also show the location of the Houston city limit, major roadways and airports, the Houston Ship Channel, and several of the largest point sources for NO_x, including petrochemical refineries (Ref), chemical plants (Chem P) and power plants (PP).

Figure 7a shows the time series of all the measurements relevant for CCN closure including the distribution of dry particle size (d_p), the C-ToF-AMS measured aerosol chemical composition and the CCNc supersaturation (blue bars). Also shown are the average measured (open circles) and predicted (solid circles) CCN concentrations assuming that the particles are composed of *i*) pure ammonium sulfate (blue), and, *ii*) a size-independent internal mixture of insoluble organics and ammonium sulfate (orange), filtered by supersaturation and concentration fluctuations and discrepancies as described earlier in the text. Particle concentrations above 10 nm measured with a TSI 3010 condensation nuclei counter are plotted (grey line) along with particle concentrations integrated from the particle size distribution measurements (blue horizontal lines). The pressure trace (black line) indicates that the whole flight occurred at a single low altitude. At the top of Figure 7a, the distribution of droplet size (D_p) is shown, which clearly shows the effect of changing supersaturation on the droplet size at the exit of the CCNc.

The particle concentration spikes observed in the first half of the flight correspond to plume transects. Starting around 2:30 PM UTC, the in-plume legs began. Two sections are highlighted with blue and pink shaded areas and correspond to when the Twin Otter first flew from and towards two point sources along the Ship Channel; Figure 7b presents these sections in higher resolution. The blue shaded area corresponds to the plume labeled “1” in Figure 6a while the pink shaded area corresponds to plume “2”. For

495 both plumes, the overprediction is greater when sampling closer to the point source, and
496 cannot be attributed to the specific internally-mixed composition assumption (since the
497 blue and the orange points lie almost on top of each other, consistent with the low volume
498 fraction of organics for this flight). Thus, we expect that the overprediction originates
499 from unresolved mixing state and composition variation with size. The improvement in
500 CCN closure further from specific point sources may imply that the aerosol composition
501 changes rapidly downwind of the aerosol source. However, the CCNc supersaturation
502 was also coincidentally higher as we sampled nearer to the point sources for these two
503 cases. It may be that the CCN closure is improved at low supersaturations
504 (corresponding to a larger d_{50}) because most of the CCN are internally-mixed, whereas
505 at higher supersaturations (corresponding to a smaller d_{50}) there are more externally-
506 mixed particles. Since the aerosol mass is weighted strongly by the particle size, another
507 possibility is that the bulk aerosol composition measured by the C-ToF-AMS does not
508 adequately represent the smaller particles, which could then have a higher organic mass
509 fraction and act less efficiently as CCN. For most of this flight, the size-resolved C-ToF-
510 AMS measurements were unable to show conclusively whether the size distribution of
511 organics is different from the sulfate size distribution (which could then be used as
512 evidence for an externally-mixed aerosol), since the organic mass loadings were quite
513 low (average for flight = 0.65 ± 0.26 μg m^{-3}).

514 Figure 8 shows that the CCN closure for the duration of RF7 is much better at
515 lower supersaturations. The color of the open circles indicates the CCNc supersaturation,
516 while the size of the markers is proportional to the concentration of particles. The
517 vertical error bars represent the effect of a 20% uncertainty in the instrument

518 supersaturation, assuming an internally-mixed composition. Ervens et al [2007] also
519 found a supersaturation-dependent overprediction bias for CCN closure at Chebogue
520 Point, Nova Scotia, attributed to undercounting in the CCNc from using a higher than
521 recommended flow rate in the CCNc. An even higher flow rate is used in this study;
522 however, the observed droplet size distribution in Figure 7b shows that the particles are
523 all above 2 μm (hence efficiently counted), demonstrating that the flow rate
524 recommendations for prevention of undercounting in the CCNc suggested by Lance et al
525 [2006] are conservative. Furthermore, in this study, CCN closure was better at low
526 supersaturations, opposite to what was seen in Ervens et al. [2007]. Thus, size-varying
527 composition (and not instrument artifacts) is likely responsible for the trend in CCN
528 prediction bias with supersaturation.
529
530 *3.5 Research Flight 22 (Sept 15, 2006)*
531 We now examine data from a flight in which sampling was carried out farther
532 from emission sources. During RF 22, backtrajectories computed with the Flexpart
533 model suggest a prevailing wind originating from the Gulf of Mexico and flowing
534 northwest over Houston; closer analysis of the trajectories (not shown) suggest the wind
535 direction changed throughout the flight, at times picking up biomass burning emissions
536 from central Texas and Louisiana. Figure 9a shows the flight track for RF22 (with marker
537 size reflecting the ambient pressure, and color, the time of day); the Twin Otter first flew
538 along the highly industrialized Ship Channel, followed by a low pass over downtown
539 Houston and several transects of the Houston plume downwind of the city. Marked on the
540 flight track are segments where particle concentrations exceed 10,000 cm^{-3} (indicating the

541 regions of highest concentrations), which occur inside the city of Houston and downwind
542 thereof. Figure 9b is similar to Figure 9a, but colored by the organic volume fraction,
543 which varies between 10% and 70% (much higher than in RF7). Figure 9b shows that
544 the organic fraction is higher downwind of Houston; the 2004 emission inventory does
545 not show any large sources for primary organic aerosol in this region, hence the organic
546 fraction increase may be associated with secondary photochemical production from urban
547 precursor emissions or mixing of regional biomass burning aerosol from central Texas.
548 The fact that the location of high organics is intersected at least three different times
549 between 7 PM and 8 PM UTC suggests a persistent feature consistent with the dominant
550 wind direction.

551 Similar to Figure 7, Figure 10 shows the time series during RF22 of measured and
552 predicted CCN concentrations for two particle chemical composition assumptions, the
553 measured aerosol size distribution, and, the measured particle composition. Compared to
554 RF7, the aerosol mass and organic volume fraction in RF22 is substantially higher.
555 Figure 10 also presents an estimate of soot mass based on the photoacoustic absorption
556 measurements. For this, the absorption coefficient (Mm^{-1}) is divided by the mass-
557 absorption efficiency (2.33 m^2 g^{-1} at 870 nm) extrapolated from a relation in Moosmuller
558 et al. [1998], assuming that all absorbing material is externally-mixed soot. This
559 approach in general would overestimate soot mass, since *i*) absorption can be enhanced
560 when internally-mixed with non-absorbing compounds [e.g., Mikhailove et al, 2006],
561 and, *ii*) a variety of organic compounds other than soot can be absorbing. However,
562 measurements from a single particle soot photometer during the concurrent TexAQS
563 campaign suggest soot loadings as high as 2 $\mu g\ m^{-3}$ in the Houston plume and a mixing-

564 state that is strongly external [Schwarz et al, 2008]. The urban soot particles observed
565 during TexAQS also show a size distribution centered around 60 nm [Schwarz et al,
566 2008], which is very close to the average d_{50} we calculate for the particles during
567 GoMACCS. Altogether, this suggests that a significant fraction of particles may be
568 externally-mixed soot that would not readily act as CCN.

569 Figure 11 shows the particle size distribution during a period of very poor CCN
570 closure (1630 cm^{-3} predicted CCN, and only 630 cm^{-3} measured CCN) on RF22 at 16:14-
571 16:18 UTC. Using the photoacoustic absorption measurement to estimate the soot mass
572 concentration as explained previously (0.7 $\mu g\ m^{-3}$ for this time period), and assuming that
573 the local maximum in the particle size distribution at 65 nm is due to an external mixture
574 of soot (consistent with the TexAQS observations), we infer a lognormal distribution of
575 soot particles (with geometric standard deviation of 1.2). Assuming that this soot
576 distribution does not contribute CCN, predicted CCN concentration drops to 720 cm^{-3},
577 which is only a 14% overprediction (as opposed to an almost 160% overprediction when
578 assuming an internal mixture without any contribution from soot). An internal-mixture
579 of soot with the other aerosol species could also decrease the number of predicted CCN
580 by reducing ε_s in the particles (i.e., increasing d_{50}). However, to explain the observed
581 CCN concentration, ε_s would need to decrease from 0.57 to 0.09 (i.e., an increase in d_{50}
582 from 50.8 nm to 94.6 nm), which is not consistent with the composition measurements
583 (with ~1 $\mu g\ m^{-3}$ sulfate and 0.8 $\mu g\ m^{-3}$ organics measured by the C-ToF-AMS at that
584 time, a lower estimate for ε_s would be ~0.38, assuming a soot density of 2 $g\ cm^{-3}$ [Slowik
585 et al, 2004]). Since soot aerosol in Houston was found to be most often externally-mixed
586 by Schwarz et al [2008], and since the photoacoustic observations onboard the Twin

587 Otter show significant absorption consistent with a large soot number concentration, we
588 are confident that an external mixture of nonhygroscopic soot aerosol is contributing to
589 the extreme CCN overprediction for this example. As the Twin Otter was sampling
590 directly downwind of the Houston Ship Channel during that time, an external mixture
591 with soot is not unexpected. However, when looking at Figure 10, there are clearly times
592 when absorption is even higher, and yet the CCN closure is good (for example, at 16:08-
593 16:11 UTC); this may result from the fact that the absorption measurements do not
594 provide the mixing-state or size distribution of the particle composition and the fact that
595 other compounds such as dust and organics can also contribute to the observed
596 absorption.

597 Due to the high mass loadings of both organics and sulfate for much of RF 22, the
598 size-resolved particle composition measurements may also provide important insight for
599 this flight. Figure 12a shows the size-resolved C-ToF-AMS measurements for the period
600 of extremely poor closure (160% CCN overprediction) at 16:14-16:17 UTC on RF 22.
601 These measurements, although noisy, confirm that the organic mass (like the soot mass)
602 is likely externally-mixed with sulfate since the size distributions of organic and sulfate
603 mass are quite dissimilar. During another period of poor closure on RF 22 (76% CCN
604 overprediction) at 16:47-16:50 UTC, the major bulk of the sulfate and organic mass
605 follow similar size distributions (Figure 12b) and the assumption of an internal mixture
606 appears to be reasonable (at least for particles larger than about 200 nm). In addition, the
607 expected soot mass during this time period is very low (the absorption is just above the
608 detection limit of the photoacoustic measurements). Both time periods shown in Figure
609 12 have similar bulk organic to sulfate ratios (0.74 ± 0.12 for period 12a and 0.87 ± 0.16

610 for period 12b). However, the CCN overprediction is much lower for the second time
611 period, and the mechanisms responsible for CCN overprediction may be different. Since
612 the aerosol appears to be internally-mixed, perhaps the effect of size-varying composition
613 is controlling the CCN overprediction for the second time period. For particles smaller
614 than about 200 nm (where many of the CCN occur), the ratio of organics to sulfate
615 appears to be much higher than for particles larger than 200 nm (where most of the mass
616 occurs); therefore, the soluble volume fraction derived from bulk composition may be
617 biased high for the majority of particles smaller than 200 nm. In order to explain the
618 number of observed CCN, the smaller particles (< 200 nm) would need to be highly
619 enriched in organics. The other possibility is that the smaller particles are much more
620 externally-mixed, which is not unexpected since many primary aerosol emission sources
621 produce extremely fine particulates. Unfortunately, it is not possible to unambiguously
622 verify the extent to which either of these mechanisms is affecting the CCN closure, since
623 the signal-to-noise ratio of the size-resolved C-TOF-AMS measurements at CCN relevant
624 sizes (between about 50 to 200 nm) is very low.

625 The CCN closure for RF 22 is shown in Figure 13, where vertical error bars
626 represent the effect of a 10% uncertainty in the instrument supersaturation on an
627 internally-mixed aerosol population. Figure 13 shows that CCN are, on average,
628 overpredicted when assuming pure ammonium sulfate aerosol (not always by the same
629 amount). On average, the closure is not better than for RF7, although the uncertainty in
630 the CCNc supersaturation is certainly lower. CCN closure improves when assuming that
631 the measured bulk organic fraction is insoluble and internally-mixed with sulfate. Under
632 more polluted conditions (higher particle concentrations), assuming the organic fraction

633 is internally-mixed results in CCN underprediction; this suggests that the organics are
634 either partially soluble or they depress droplet surface tension (thereby facilitating droplet
635 activation and increasing CCN concentrations).

636 The underlying message is that the details of particle composition (e.g. size-
637 resolved chemical composition, surfactant properties and mixing-state) are fundamental
638 for successful CCN closure in close proximity to emission sources, especially for such a
639 complex environment as Houston.

640

641 *3.6 Kinetics of Droplet Growth*

642 Figure 14 shows the average droplet diameter at the exit of the CCNc column for
643 all flights as a function of the CCNc supersaturation. For comparison, we show the
644 average droplet diameter for classified ammonium sulfate particles exposed to a range of
645 supersaturations in the laboratory at 1 L min^{-1} total flow rate (dashed line in Figure 13).
646 We vary the dry ammonium sulfate particle size from 10 nm to over 200 nm during the
647 calibration to obtain the range of droplet sizes expected for a given supersaturation (grey
648 shaded region in Figure 13). On average, the droplet diameter from ambient
649 measurements is above the lower limit established by the calibration aerosol. Since the
650 critical supersaturation of the ambient particles is unknown, the droplet size cannot be
651 unambiguously related to the growth rate. The droplet growth rate is driven by the
652 difference between the instrument supersaturation and the particle equilibrium
653 supersaturation, and is also proportional to the amount of time the droplets are given to
654 grow upon activation. Particles that activate at a lower supersaturation than the
655 instrument supersaturation will have both a higher driving force for condensational

656 growth and more time to grow (as they will activate even before supersaturation has fully
657 developed in the instrument). Another factor influencing the droplet growth rate is the
658 number of CCN present in the column, which can deplete the water vapor at very high
659 particle concentrations. The ammonium sulfate calibrations supplied no greater than 600
660 cm^{-3} CCN at any given time; therefore, we expect that comparisons with ambient
661 measurements having much higher CCN concentrations (and, therefore, potentially
662 smaller droplet sizes) may bias our assessment of the droplet growth rate. However,
663 Figure 13 supports that all droplets formed from ambient aerosol are, on average, larger
664 than the droplet formed from calibration aerosol. This comparison, termed "Threshold
665 Droplet Growth Analysis", suggests that significant water vapor depletion does not occur
666 within the CCNc, even with CCN concentrations up to 10,000 cm^{-3}. Furthermore,
667 droplets on average do not grow more slowly than activated ammonium sulfate particles,
668 which suggests that the presence of organics, for the range of supersaturations
669 considered, does not substantially delay the activation kinetics of CCN. This is contrary
670 to the findings of Ruehl et al [2008] who report up to 62% of the particles having
671 moderate kinetic inhibition to condensational growth at a ground-based site in Houston
672 during GoMACCS, using a Phase Doppler Interferometer to monitor the droplet size in
673 another continuous-flow streamwise thermal gradient CCN chamber. The apparent
674 discrepancy between this study and Ruehl et al [2008] motivates future side-by-side
675 comparisons of the instruments to establish whether observed differences arise from
676 differences in sampled particle phase state, or artifacts from the optical detection or
677 thermal processing of the aerosol in either of the instruments [Asa-Awuku et al., 2008b].
678

4. Conclusions

This study provides an airborne CCN closure analysis in a heavily polluted environment. Average CCN concentrations ranged from 100 cm^{-3} to more than 10,000 cm^{-3}, and organic volume fraction in the aerosol were as high as 70%. The results show that CCN closure is overall attainable with an average overprediction bias of 36%, by simply assuming it to be composed of pure ammonium sulfate. Accounting for the internally-mixed particle soluble volume fraction, estimated from the sulfate and organic mass loadings, reduces the average overprediction bias to 3%. Even when the first-order behavior of CCN is well constrained by simple volume fraction assumptions, the scatter between predicted and observed CCN concentrations remains large. Simultaneous measurements of size-resolved composition and mixing-state as well as surfactant properties of the aerosol are required to reduce the uncertainty in CCN closure for such a heterogeneous mix of pollution sources. Contrary to ground-based measurements in the Houston area, the activation kinetics of the CCN are always similar to ammonium sulfate, and do not suggest delays from the presence of organics.

695 ***Acknowledgements***

696 We acknowledge support from the National Oceanic and Atmospheric
697 Administration (NOAA) under contracts NA05OAR4310101 and NA06OAR4310082,
698 the support of an NSF CAREER grant, and the Office of Naval Research. SL would like
699 to acknowledge the support of a Georgia Institute of Technology (Georgia Tech)
700 Presidential Fellowship and a National Center for Atmospheric Research (NCAR)
701 Advanced Study Program (ASP) Graduate Fellowship. We also thank C.Brock and three
702 anonymous reviewers for helpful comments, as well as A Stohl and S. Ekhardt for
703 providing the Flexpart backtrajectory results.

704 **References**

705 Arnott, W. P. and Moosmüller, H., Real time, in situ measurement of aerosol light
706 absorption with a new photoacoustic instrument. *Instr. Aerosp. Indus*., 44, 713, 1998.

707 Arnott, W. P. et al., Photoacoustic spectrometer for measuring light absorption by
708 aerosol: instrument description. *Atmos. Environ*., 33 (17), 2845, 1999.

709 Arnott, W. P. et al., Photoacoustic insight for aerosol light absorption aloft from
710 meteorological aircraft and comparison with particle soot absorption photometer
711 measurements: DOE Southern Great Plains climate research facility and the coastal
712 stratocumulus imposed perturbation experiments. *J. Geophy. Res*., 111 (D5), 2006.

713 Asa-Awuku, A., Nenes, A., Sullivan, A.P., Hennigan, C.J. and Weber, R.J., Investigation
714 of molar volume and surfactant characteristics of water-soluble organic compounds in
715 biomass burning aerosol, *Atmos. Chem. Phys.*, 8, 799-812, 2008a

716 Asa-Awuku, A., Engelhart, G.J., Lee, B.H., Pandis, S.N., and Nenes, A., Relating CCN
717 activity, volatility, and droplet growth kinetics of β-caryophyllene secondary organic
718 aerosol*, Atmos. Chem. Phys. Discuss.*, 8, 10105-10151, 2008b

719 Asa-Awuku, A.A., Moore, R.H., Brock, C.A., Bahreini, R., Middlebrook, A.M.,
720 Schwarz, J.P., Spackman, J.R., Holloway, J.S., Stickel, R., Tanner, D.J., Huey, L.G.,
721 Nenes, A., Airborne Cloud Condensation Nuclei Measurements during the 2006 Texas
722 Air Quality Study, *J. Geoph. Res.*, in review

723 Bahreini, R., J. L. Jimenez, J.Wang, R. C. Flagan, J. H. Seinfeld, J. T. Jayne, and D. R.
724 Worsnop, Aircraft-based aerosol size and composition measurements during ACE-Asia
725 using an Aerodyne aerosol mass spectrometer, *J. Geophys. Res*., 108 (D23), 8645, 2003.

726 Broekhuizen, K., R.Y.W, Chang, W.R. Leaitch, S.M. Li, J.P.D. Abbatt, Closure between
727 measured and modeled cloud condensation nuclei (CCN) using size-resolved aerosol
728 compositions in downtown Toronto, *Atmos. Chem. Phys.*, 6: 2513-2524, 2006.

729 Cantrell, W., G. Shaw, G.R. Cass, Z. Chowdhury, L.S. Hughes, K.A. Prather, S.A.
730 Guazzotti, K.R. Coffee, Closure between aerosol particles and cloud condensation nuclei
731 at Kaashidhoo Climate Observatory, *J. Geophys. Res.*, 106 (D22), 28711-28718, 2001.

732 Chan, M.N., S.M. Kreidenweis and C.K. Chan, Measurements of the Hygroscopic and
733 Deliquescence Properties of Organic Compounds of Different Solubilities in Water and
734 Their Relationship with Cloud Condensation Nuclei Activities, *Environ. Sci. Technol*.,
735 42, 3602–3608, 2008.

736 Chang, R.Y.-W., P.S.K. Liu, W.R. Leaitch, J.P.D. Abbatt, Comparison between
737 measured and predicted CCN concentrations at Egbert, Ontario: Focus on the organic
738 aerosol fraction at a semi-rural site, *Atmos. Environ*., 41, 8172–8182, 2007.

739 Cubison, M.J., B. Ervens, G. Feingold, K.S. Docherty, I.M. Ulbrich, L. Shields, K.
740 Prather, S. Hering and J.L. Jimenez, The influence of chemical composition and mixing
741 state of Los Angeles urban aerosol on CCN number and cloud properties, *Atmos. Chem.*
742 *Phys*., 8, 5649–5667, 2008.

743 Decesari, S., M.C. Facchini, S. Fuzzi, G.B. McFiggans, H. Coe and K.N. Bower, The
744 water-soluble organic component ofsize-segregated aerosol, cloud water and wet
745 depositions from Jeju Island during ACE-Asia, *Atmos. Environ*., 39, 211–222, 2005.

746 E. Dinar, T.F. Mentel and Y. Rudich, The density of humic acids and humic like
747 substances (HULIS) from fresh and aged wood burning and pollution aerosol particles,
748 *Atmos. Chem. Phys*., 6, 5213–5224, 2006.

749 Dinar, E., T. Anttila and Y. Rudich, CCN Activity and Hygroscopic Growth of Organic
750 Aerosols Following Reactive Uptake of Ammonia, *Environ. Sci. Tech*nol., 42, 793-799,
751 2008.

752 Drewnick, F., Hings, S. S., DeCarlo, P., Jayne, J. T., Gonin, M., Fuhrer, K., Weimer, S.,
753 Jimenez, J. L., Demerjian, K. L., Borrmann, S., Worsnop, D. R. A new time-of-flight
754 aerosol mass spectrometer (TOF-AMS) - instrument description and first field
755 deployment., *Aeros. Sci. Technol*., 2005, 39, 637-658.

Dusek, U., G.P. Frank, L. Hildebrandt, J. Curtius, J. Schneider, S. Walter, D. Chand, F. Drewnick, S. Hings, D. Jung, S. Borrmann, M.O. Andreae, Size Matters More Than Chemistry for Cloud-Nucleating Ability of Aerosol Particles, *Science*, 312, 2006.

Engelhart, G.J., Asa-Awuku, A., Nenes, A., and Pandis, S.N., CCN activity and droplet growth kinetics of fresh and aged monoterpene secondary organic aerosol, *Atmos. Chem. Phys.,* 8, 3937-3949, 2008.

Ervens, B., M. Cubison, E. Andrews, G. Feingold, J.A. Ogren, J.L. Jimenez, P. DeCarlo, A. Nenes, Prediction of cloud condensation nucleus number concentration using measurements of aerosol size distributions and composition and light scattering enhancement due to humidity, *J. Geophys. Res.*, 112 (D10), D10S32, 2007.

Facchini, M.C., S. Decesari, M. Mircea, S. Fuzzi and G. Loglio, Surface tension of atmospheric wet aerosol and cloud/fog droplets in relation to their organic carbon content and chemical composition, *Atmos. Environ*., 34, 4853-4857, 2000.

Furutani, H., M. Dall'osto, G.C. Roberts, K.A. Prather, Assessment of the relative importance of atmospheric aging on CCN activity derived from field observations, *Atmos. Environ*., 42, 3130-3142, 2008.

Hegg, D. A., D. S. Covert, P. A. Covert, and H. Jonsson, Determination of the efficiency of an aircraft aerosol inlet, *Aerosol Sci. Technol*., 39, 966– 971, 2005

Hinds, W.C., Properties, behavior, and measurement of airborne particles, John Wiley and Sons, Inc, 1999.

IPCC (Intergovernmental Panel on Climate Change): *Changes atmospheric constituents and in radiative forcing in: Climate change 2007: The physical science basis*, Cambridge University Press, 2007.

Lance, S., J. Medina, J. N. Smith, and A. Nenes, Mapping the operation of the DMT continuous flow CCN counter, *Aerosol Sci. Technol*., 40 (4), 242–254, 2006.

781 Lu, M-L, G. Feingold, H.H. Jonsson, P.Y. Chuang, H. Gates, R.C. Flagan, J.H. Seinfeld,
782 Aerosol-cloud relationships in continental shallow cumulus, *J. Geophys. Res*., 113,
783 D15201, doi:10.1029/2007JD009354, 2008.

784 Medina, J., A. Nenes, R.E.P. Sotiropoulou, L.D. Cottrell, L.D. Ziemba, P.J. Beckman,
785 R.J. Griffin, Cloud condensation nuclei closure during the International Consortium for
786 Atmospheric Research on Transport and Transformation 2004 campaign: Effects of size-
787 resolved composition, *J. Geophys. Res.*, 112 (D10), D10S31, 2007.

788 Mircea, M., M.C. Facchini, S. Decesari, F. Cavalli, L. Emblico, S. Fuzzi, A. Vestin, J.
789 Rissler, E. Swietlicki, G. Frank, M.O. Andreae,W. Maenhaut, Y. Rudich and P. Artaxo,
790 Importance of the organic aerosol fraction for modeling aerosol hygroscopic growth and
791 activation: a case study in the Amazon Basin, *Atmos. Chem. Phys*., 5, 3111–3126, 2005.

792 Moosmüller, H. et al., Photoacoustic and filter measurements related to aerosol light
793 absorption during the Northern Front Range Air Quality Study (Colorado 1996/1997). *J.*
794 *Geophys. Res*., 103 (D21), 28149, 1998.

795 Murphy, S. M., Agrawal, H, Sorooshian, A, Padró, L.T., Gates, H., Hersey, S., Welch,
796 W.A., Jung, H., Miller, J. W., Cocker, D.R., Nenes, A., Jonsson, H., Flagan, R.C,
797 Seinfeld, J.H., "Comprehensive simultaneous shipboard and airborne characterization of
798 exhaust from a modern container ship at sea." *Environ. Sci. Technol.*, Article ASAP,
799 DOI: 10.1021/es802413j, 2009.

800 Nenes, A. and Medina, J., Scanning Mobility CCN Analysis - A method for fast
801 measurements of size-resolved CCN activity and growth kinetics, *Aerosol Sci. Technol.*,
802 in review

803 Nenes, A., R.J. Charlson, M.C. Facchini, M. Kulmala, A. Laaksonen and J.H. Seinfeld,
804 Can chemical effects on cloud droplet number rival the first indirect effect? *Geophys.*
805 *Res. Lett*., 29, 1848, doi:10.1029/2002GL015295, 2002.

806 Noone, K.J., J.A. Ogren, J. Heintzenberg, R.J. Charlson and D.S. Covert, Design and
807 calibration of a counterflow virtual impactor for sampling of atmospheric fog and cloud
808 droplets, *Aeros. Sci. Tech*., 8, 3, 235-244, 1988.

809 Ogren, J.A., J. Heintzenberg, A. Zuber, K.J. Noone, and R.J. Charlson, Measurements of
810 the size-dependence of non-volatile aqueous mass concentrations in cloud droplets.
811 *Tellus*, 41B, 24-31, 1992.

812 Padró, L.T., Asa-Awuku, A., Morrison, R., and A. Nenes, Inferring thermodynamic
813 properties from CCN activation experiments: single-component and binary aerosols,
814 Atmos. Chem. Phys., 7, 5263-5274, 2007

815 Petters, M.D. and Kreidenweis, S.M., A single parameter representation of hygroscopic
816 growth and CNN activity, *Atmos. Chem. Phys.*, 7, 1961-1971, 2007.

817 Quinn, P.K., T.S. Bates, D.J. Coffman and D.S. Covert, Influence of particle size and
818 chemistry on the cloud nucleating properties of aerosols, *Atmos. Chem. Phys*., 8, 1029-
819 1042, 2008.

820 Roberts, G., and Nenes, A., A Continuous-Flow Longitudinal Thermal-Gradient CCN
821 Chamber for Atmospheric Measurements, *Aeros.Sci.Tech.*, 39, 206–221,
822 doi:10.1080/027868290913988, 2005

823 Rose, D., S.S. Gunthe, E. Mikhailov, G.P. Frank, U. Dusek, M.O. Andreae, U.Poschl,
824 Calibration and measurement uncertainties of a continuous-flow cloud condensation
825 nuclei counter (DMT-CCNC): CCN activation of ammonium sulfate and sodium chloride
826 aerosol particles in theory and experiment, *Atmos. Chem. Phys*., 2008.

827 Ruehl, C.R., Chuang, P.Y., and Nenes, A., How quickly do cloud droplets form on
828 atmospheric particles, *Atmos.Chem.Phys.*, 8, 1043-1055, 2008

829 Salcedo, D., Equilibrium Phase Diagrams of Aqueous Mixtures of Malonic Acid and
830 Sulfate/Ammonium Salts, *J. Phys. Chem*., 110, 12158-12165, 2006.

831 Saxena, P., and L. M. Hildemann, Water-soluble organics in atmospheric particles: A
832 critical review of the literature and application of thermodynamics to identify candidate
833 compounds, *J. Atmos. Chem.*, 24, 57– 109, 1996.

834 Schwarz, J.P., R.S. Gao, J.R. Spackman, L.A. Watts, D.S. Thomson, D.W. Fahey, T.B.
835 Ryerson, J. Peischl, J.S. Holloway, M. Trainer, G.J. Frost, T. Baynard, D.A. Lack, J.A. de
836 Gouw, C. Warneke, and L.A. Del Negro, Measurement of the mixing state, mass and
837 optical size of individual black carbon particles in urban and biomass burning emissions,
838 *Geophys. Res. Lett*., 35, L13810, doi:10.1029/2008GL033968, 2008.

839 Seinfeld, J.H. and Pandis, S.N. *Atmospheric Chemistry and Physics: From Air Pollution*
840 *to Climate Change*, Wiley, 2nd Ed., 2006

841 Shulman, M.L., M.C. Jacobson, R.J. Carlson, R.E. Synoveca and T.E. Young,
842 Dissolution behavior and surface tension effects of compounds in nucleating cloud
843 droplets, *Geophys. Res. Lett.*., 23, 3, 277-280, 1996.

844 Slowik, J.G., K. Stainken, P. Davidovits, L.R. Williams, J.T. Jayne, C.E. Kolb, D.R.
845 Worsnop, Y. Rudich, P.F. DeCarlo and J.L. Jimenez, Particle Morphology and Density
846 Characterization by Combined Mobility and Aerodynamic Diameter Measurements. Part
847 2: Application to Combustion-Generated Soot Aerosols as a Function of Fuel
848 Equivalence Ratio, *Aeros Sci. Technol.*, 38:1206–1222, 2004.

849 Sorooshian, A., S. Hersey, F.J. Brechtel, A. Corless, R.C. Flagan, J.H. Seinfeld, Rapid,
850 size-resolved aerosol hygroscopic growth measurements: Differential aerosol sizing and
851 hygroscopicity spectrometer probe (DASH-SP), *Aeros. Sci. Tech*., 42, 6, 445-464, 2008b.

852 Sorooshian, A., Murphy, S. M., Hersey, S., Gates, H., Padro, L. T., Nenes, A., Brechtel,
853 F. J., Jonsson, H., Flagan, R. C., Seinfeld, J. H., "Comprehensive airborne
854 characterization of aerosol from a major bovine source." *Atmos. Chem. Phys. Discus.*, 8,
855 10415-10479.

856 VanReken, T.M., T.A. Rissman, G.C. Roberts, V. Varutbangkul, H.H. Jonsson, R.C.
857 Flagan, J.H. Seinfeld, Toward aerosol/cloud condensation nuclei (CCN) closure during
858 CRYSTAL-FACE , *J. Geophys. Res.*, 108 (D20): Art. No. 4633, 2003.

859 Vestin A, Rissler J, Swietlicki E, et al., Cloud-nucleating properties of the Amazonian
860 biomass burning aerosol: Cloud condensation nuclei measurements and modeling, *J.*
861 *Geophys. Res.*, 112 (D14): Art. No. D14201, 2007.

862 Wang , J., R. C. Flagan, and J. H. Seinfeld, A differential mobility analyzer DMA)
863 system for submicron aerosol measurements at ambient relative humidity, *Aerosol Sci.*
864 *Technol*., 37, 46– 52, 2003.
865 Zelenyuk, Cai and Imre. From Agglomerates of Spheres to Irregularly Shaped Particles:
866 Determination of Dynamic Shape Factors from Measurements of Mobility and Vacuum
867 Aerodynamic Diameters," submitted to *Aeros. Sci. Tech,* 2005.

868

869 **Table 1.** Twin Otter Science Flights During GoMACCS. Note CCN data in first 3
870 Flights are not available.
871

Flight	Date	Mission Description	Wind Direction (from)	AMS Data Used?	Super-Saturation Range [%]	CCN Concentration Range [cm^{-3}]
RF 1	8/21	Parish coal PP	E-SE	No	-	-
RF 2	8/22	Parish coal PP	E	No	-	-
RF 3	8/23	Parish coal PP	E	No	-	-
RF 4	8/25	Ship Channel	S-SE, NE	No	0.35-0.7	250-5,000
RF 5	8/26	Conroe	S, N-NE	No	0.4-0.7	200-800
RF 6	8/27	Beaumont	S-SE	Yes	0.3-0.5	200-1,000
RF 7	8/28	Baytown	SW	Yes	0.5-1.0	500-5,000
RF 8	8/28		S	No	-	-
RF 9	8/29	Parish coal PP	W-NW	No	0.55-1.0	200-3,000
RF 10	8/31		N-NW	No	0.5-0.55	600-6,000
RF 11	9/1	Houston, Ship Channel	N	No	0.35-0.85	250-10,000
RF 12	9/2	Local BB	N-NE	Yes	0.5-0.55	600-9,000
RF 13	9/3	Houston, Parish coal PP	NE	No	0.45-0.5	1,500-15,000
RF 14	9/4	Parish coal PP	NE, NW	Yes	0.5-0.55	400-3,000
RF 15	9/6	Waste Treatment	N-NE	Yes	0.5-0.6	200-5,000
RF 16	9/7	Galveston	NE	Yes	0.35-0.9	200-6,000
RF 17	9/8	Parish coal PP	E-NE, W	No	0.4-0.9	250-9,000
RF 18	9/10		S	No	-	-
RF 19	9/11	Fayette coal PP	S, NW	No	0.45-0.55	150-1,000
RF 20	9/13	Conroe	N	No		350-7,000
RF 21	9/14	Houston, Parish	E-NE	Yes	0.45-0.55	200-15,000
RF 22	9/15	Houston	S-SE	Yes	0.45-0.55	300-8,000

872 PP = Power Plant
873 BB = Biomass Burning
874

875 **Table 2.** Summary of CCNc operation characteristics. Refer to explanation of "Flight
876 Category" in text.

Flight	IPC On?	Flow-Restrictor Present?	Flight Category	ΔT variance [^{o}C]	Q_{sh} variance [cc min^{-1}]	P variance [mbar]	SS variance [%]
RF 4	No	No	2	0.50	19.4128	1.226	0.064
RF 5	No	Yes	2	0.34	5.90161	1.657	0.052
RF 6	No	Yes	2	0.06	4.71778	1.735	0.008
RF 7	No	No	1	0.73	19.6443	1.068	0.095
RF 9	No	Yes	2	0.76	3.51723	1.003	0.087
RF 10	Yes	Yes	4	0.01	5.46324	1.906	0.003
RF 11	Yes	Yes	3	0.01	5.44902	0.201	0.002
RF 12	Yes	Yes	4	0.01	5.06662	1.669	0.002
RF 13	Yes	Yes	4	0.01	5.61638	0.263	0.003
RF 14	Yes	Yes	4	0.01	5.15539	1.639	0.003
RF 15	Yes	Yes	4	0.01	4.43912	1.800	0.003
RF 16	Yes	Yes	3	0.01	5.55128	0.909	0.003
RF 17	Yes	Yes	3	0.01	4.88951	1.040	0.004
RF 19	Yes	Yes	4	0.01	4.84348	1.514	0.003
RF 20	Yes	Yes	4	0.01	4.94734	2.042	0.003
RF 21	Yes	Yes	4	0.01	4.07664	1.886	0.003
RF 22	Yes	Yes	4	0.01	4.31556	1.600	0.003

877
878

Figure Captions

Figure 1. (a) Flight tracks for the Twin Otter research flights (RF) during which CCN measurements were available. (b) Photograph of the Twin Otter (with the main inlet and CVI inlet indicated), over a photograph of the industries along the Houston Ship Channel.

Figure 2. CCNc operating conditions (pressure, temperature and supersaturation) for four representative flights.

Figure 3. 1Hz CCN observations obtained during this study plotted as a (a) function of ambient pressure and time (exposed to a range of supersaturations, from 0.3% to 1.0%), and, (b) supersaturation range histogram. Total CCN are plotted as the solid black line.

Figure 4. CCN closure for all flights, assuming pure ammonium sulfate aerosol. The thick solid line shows the 1:1 relationship, and the grey bands indicate over- and under-prediction by factors of 2-4. Symbols are colored with respect to research flight number (top panel, a), and instrument supersaturation (lower panel, b). The dashed line in the lower panel shows the best fit relationship with the given equation.

Figure 5. CCN closure for select flights, using bulk particle composition from the C-ToF-AMS. Symbols indicate the particle composition assumption in the CCN concentration calculation; black "+" symbols correspond to pure ammonium sulfate, colored points assume an internal mixture of sulfate and insoluble organic with 1.4 g cm^{-3} density and surface tension of pure water, grey "+" symbols indicate the same assumptions about organic mass and also a 15 mN m^{-1} reduction in surface tension. Symbols are colored by flight number (top panel, a), and instrument supersaturation (lower panel, b). The dashed line in the lower panel gives the linear best fit slope (with zero offset) assuming ammonium sulfate for all flights, while the red solid line gives the linear best fit slope (with zero offset) assuming an internal mixture based on the bulk composition for the flights listed in 5a.

Figure 6. Flight track for RF7. Aircraft position colored by (a) flight time; sections with particle concentrations (with diameter larger than 10nm) greater than 10,000 cm^{-3} are shown in greyscale, and, (b) aerosol organic volume fraction (calculated as explained in the text). Map scale is approximately 50 miles across.

Figure 7. Time-series for RF7 of measured and predicted CCN concentrations, particle concentrations with d_p > 10nm, ambient pressure and AMS measured mass loadings of sulfate, organic, nitrate and ammonium ions. At the top are image plots of dry particle diameter (d_p) and droplet diameter (D_p) size distributions, colored by the bin-normalized concentrations (colorbar not shown). The CCNc supersaturation is plotted as bars. Blue and pink shaded areas depict regions of interest, as described in the text. Results shown for the whole flight (top panel, a), and, for data collected between 2:55 PM and 3:23 PM (bottom panel, b)

Figure 8. CCN closure for RF7 with different assumptions about particle chemistry. Colors represent the CCNc supersaturation and marker size reflects the ambient particle concentrations. Vertical error bars are based on a supersaturation uncertainty of 20%. Dashed lines indicate under- and over-prediction by 100%.

Figure 9. Flight track for RF22. Aircraft position colored by (a) flight time, with line thickness proportional to the ambient pressure (lower altitude legs have a thicker line); sections when particle concentrations (with diameter larger than 10nm) are greater than 10,000 cm^{-3} are shown in grayscale, and, (b) organic volume fraction, calculated as described in the text. Map scale is approximately 50 miles across.

Figure 10. Time-series for RF22 of measured and predicted CCN concentrations, particle concentrations with d_p > 10 nm, ambient pressure and AMS measured mass loadings of sulfate, organic, nitrate and ammonium ions. Also shown is the soot mass estimated from the photoacoustic absorption measurements. At the top are image plots of dry particle diameter (d_p) and droplet diameter (D_p) size distributions, colored by the bin-normalized concentrations (colorbar not shown). The CCNc supersaturation is plotted as bars. Vertical gray bars indicate time periods when the counterflow virtual impactor was turned on.

Figure 11. Particle size distribution (red bars) during a period of very high CCN overprediction on RF22 (at 16:10-16:18 UTC). Soot size distribution (blue bars) assuming a lognormal distribution with mean diameter of 65 nm, with particle number concentration constrained using estimated soot mass concentrations from photoacoustic absorption measurements. Vertical solid line indicates the smallest particle size expected

938 to activate, d_{50}, given the assumptions of internally-mixed aerosol composition. The
939 horizontal error bar shows the effect of a 10% supersaturation uncertainty on d_{50} under
940 the same assumptions.

941 **Figure 12.** Size-resolved chemical composition measured by the C-TOF-AMS during
942 RF 22, a) at 16:14-16:18 UTC (160% CCN overprediction), and b) at 16:47-16:50 UTC
943 (76% CCN overprediction). $dM/dlogD_{va}$ is the observed mass for each size bin
944 normalized by the bin width (in log-space) of vacuum aerodynamic diameter.

945 **Figure 13.** CCN closure for RF22 with different assumptions for particle composition.
946 Higher organic volume fractions (represented by redder markers) are correlated with
947 higher CCN and particle concentrations. Vertical error bars are based on a
948 supersaturation uncertainty of 10%. Dashed lines indicate under- and over-prediction by
949 100%.

950 **Figure 14.** Average droplet diameter at the exit of the CCNc as a function of the
951 instrument supersaturation for all ambient CCN measurements during the campaign. The
952 gray shaded area indicates one standard deviation of the calibrations with ammonium
953 sulfate aerosol.
954

955 **Figure 1.**
956

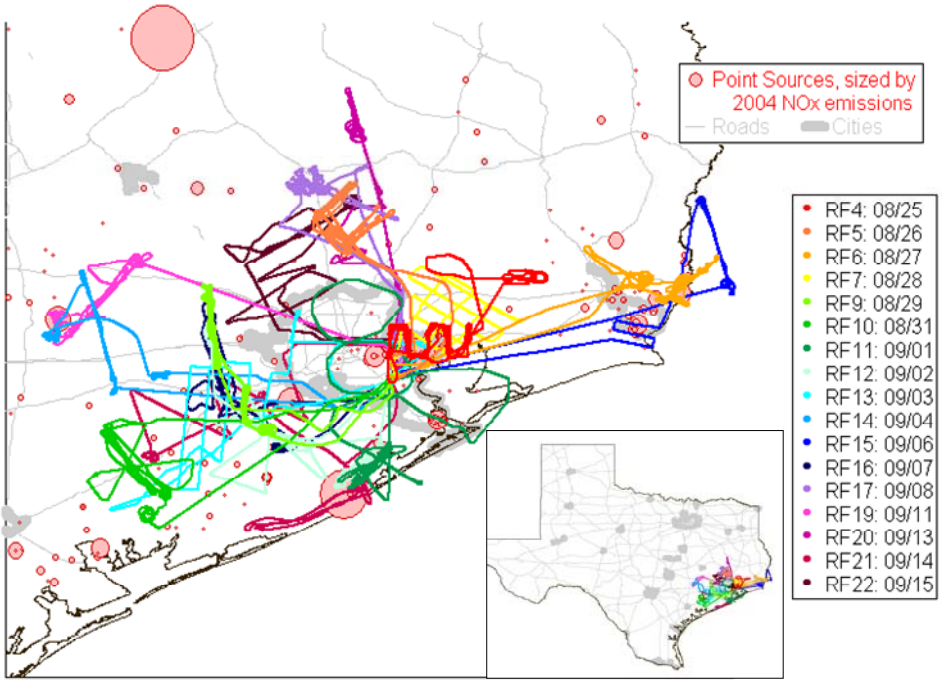

957
958 **(a)**
959

960
961 **(b)**
962
963

964 **Figure 2.**

965

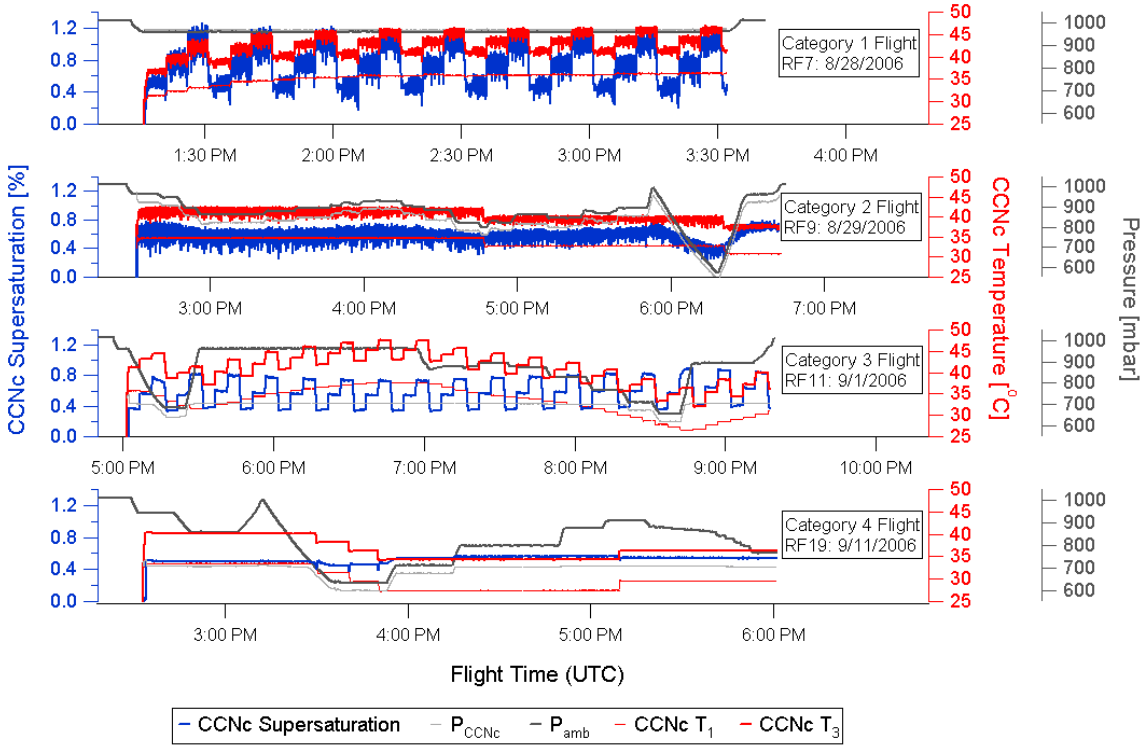

966

967 **Figure 3.**
968

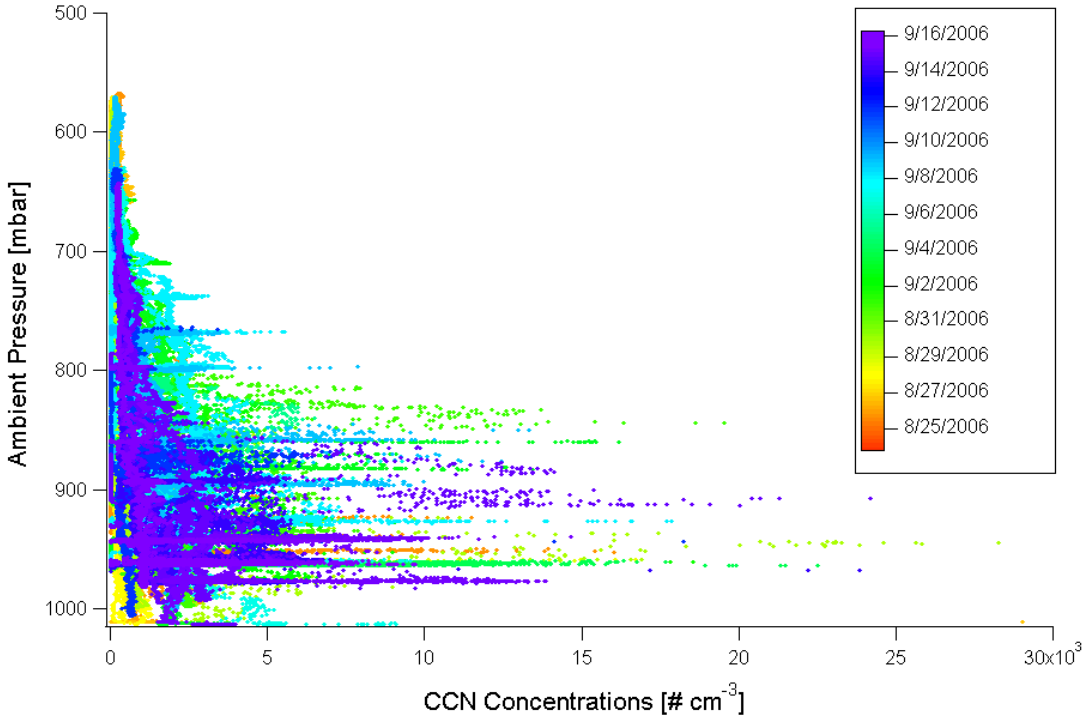

969
970 **(a)**
971

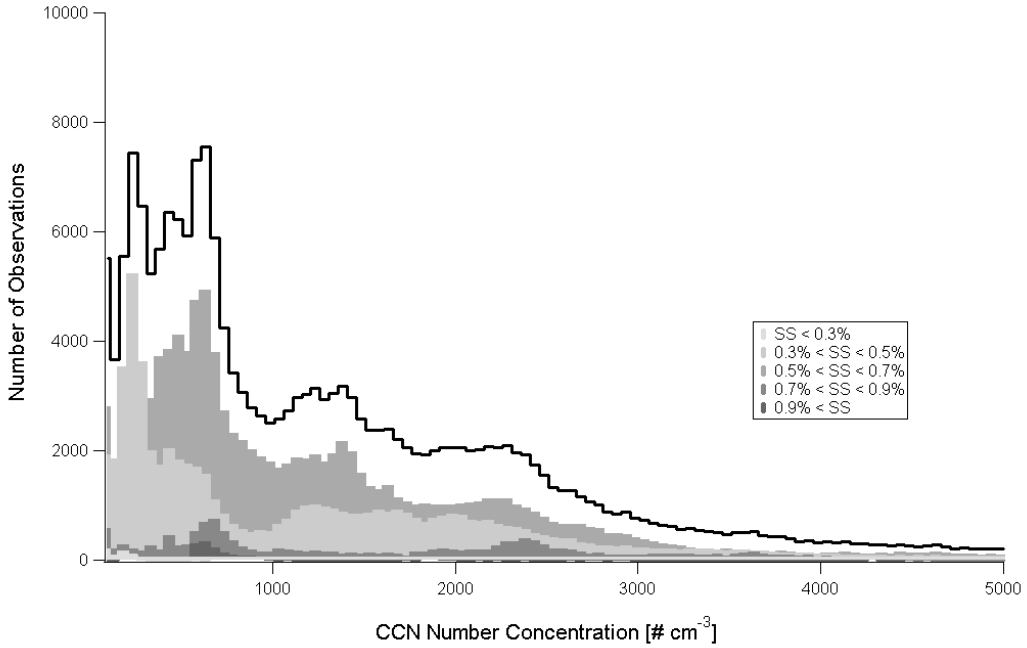

972
973 **(b)**
974

975 **Figure 4.**
976

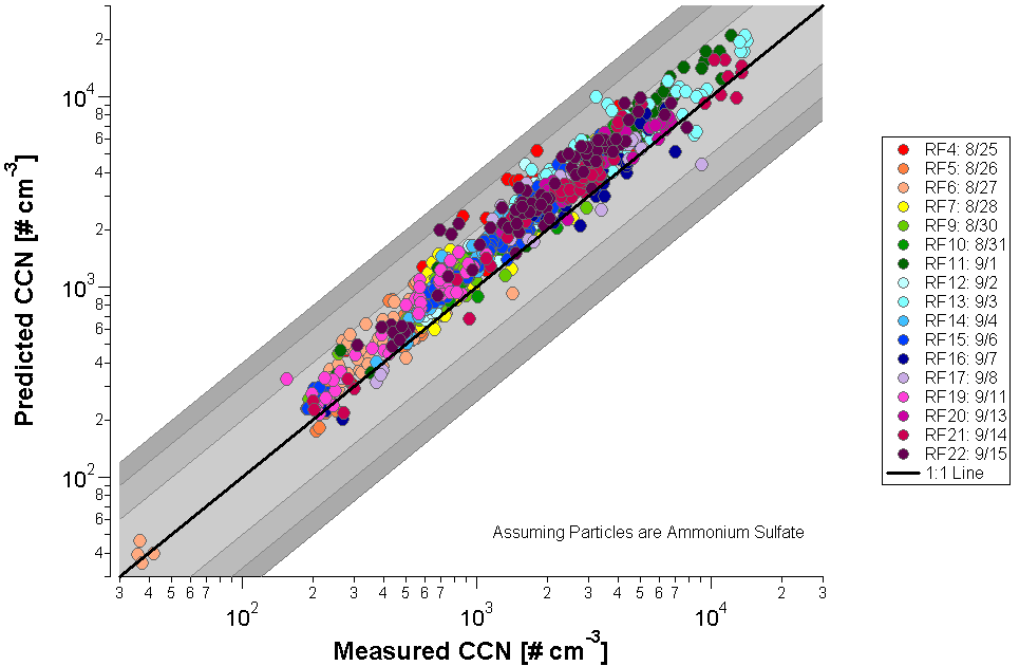

977
978
979 **(a)**
980
981
982

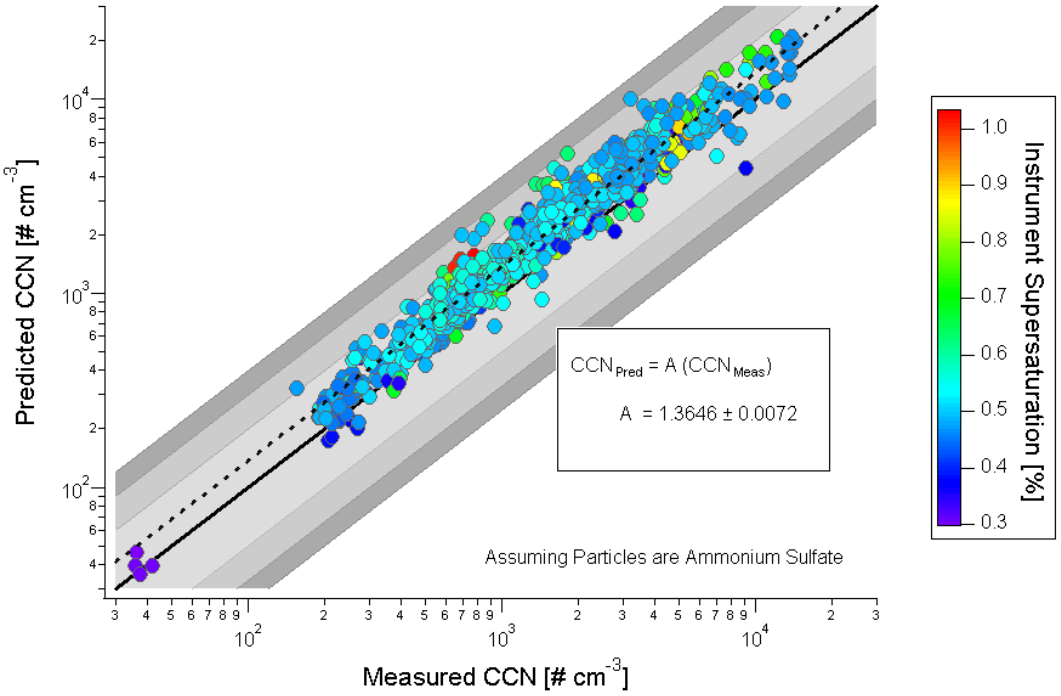

983
984
985 **(b)**

986 **Figure 5.**
987

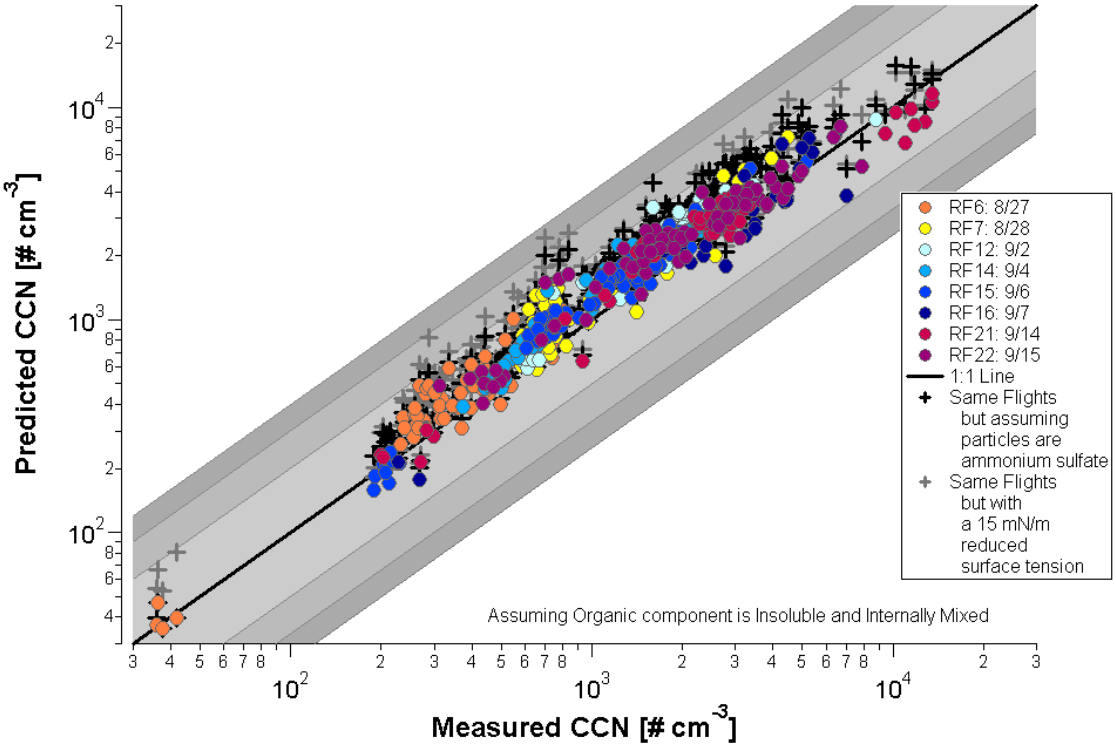

988
989 **(a)**
990
991

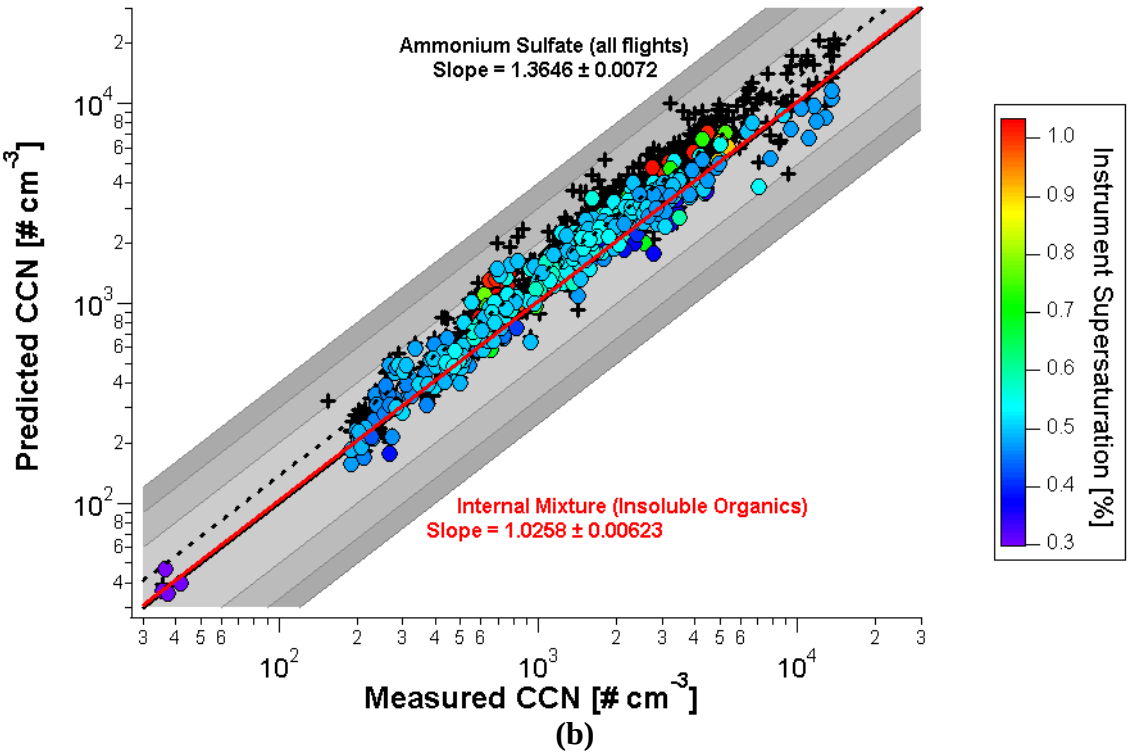

992
993 **(b)**

994 **Figure 6.**

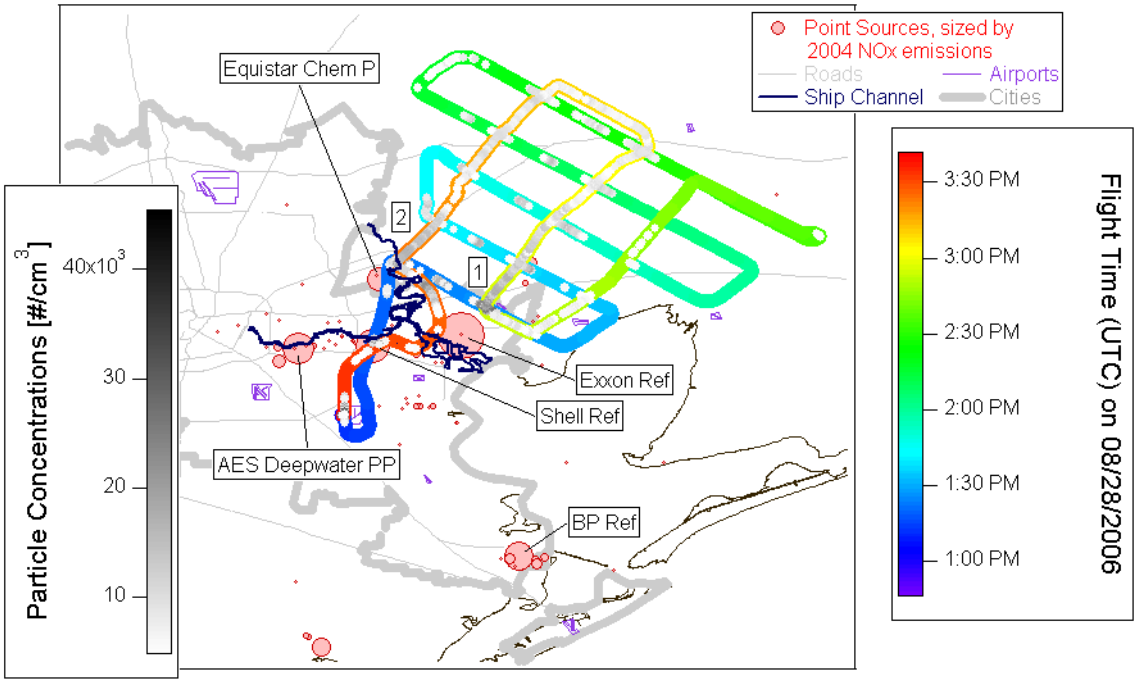

995
996 **(a)**
997

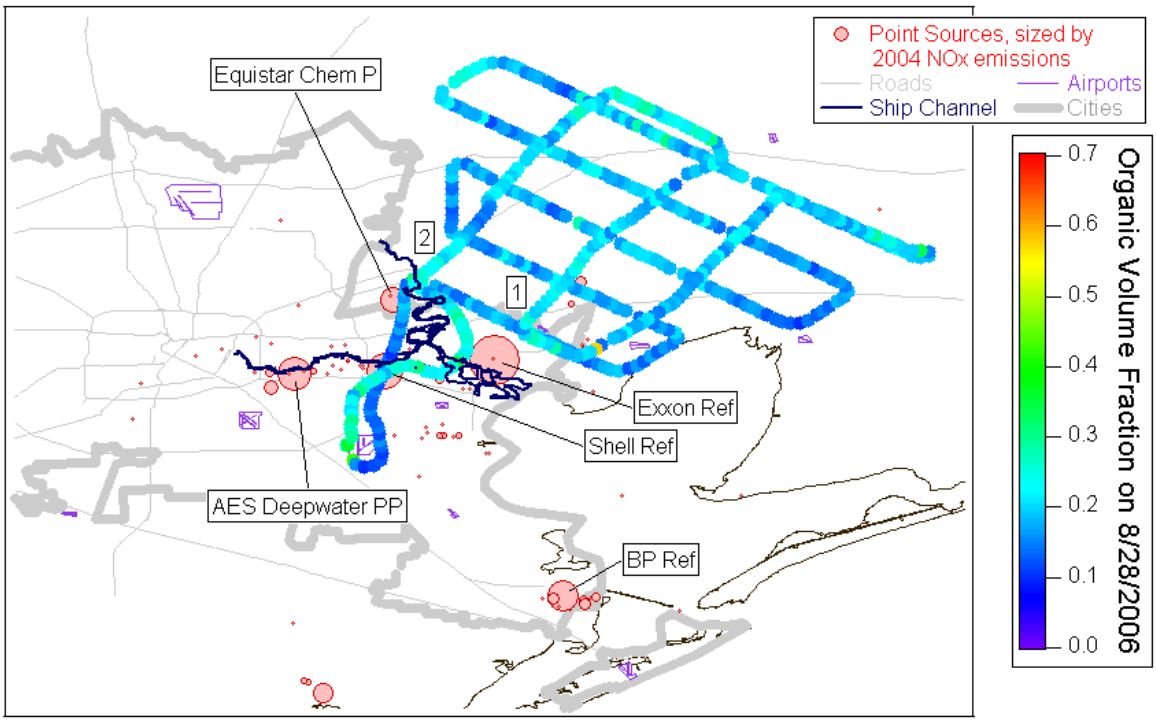

998
999 **(b)**

Figure 7.

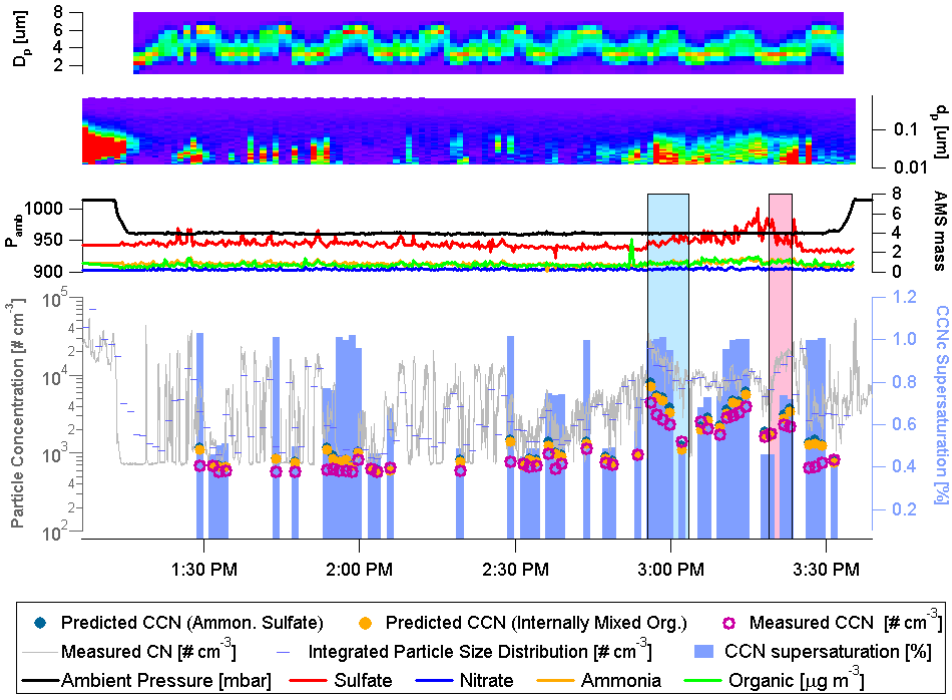
D_p [um]
d_p [um]
P_amb
AMS mass
Particle Concentration [# cm^-3]
CCNc Supersaturation [%]
1:30 PM
2:00 PM
2:30 PM
3:00 PM
3:30 PM
Predicted CCN (Ammon. Sulfate)
Predicted CCN (Internally Mixed Org.)
Measured CCN [# cm^-3]
Measured CN [# cm^-3]
Integrated Particle Size Distribution [# cm^-3]
CCN supersaturation [%]
Ambient Pressure [mbar]
Sulfate
Nitrate
Ammonia
Organic [μg m^-3]

(a)

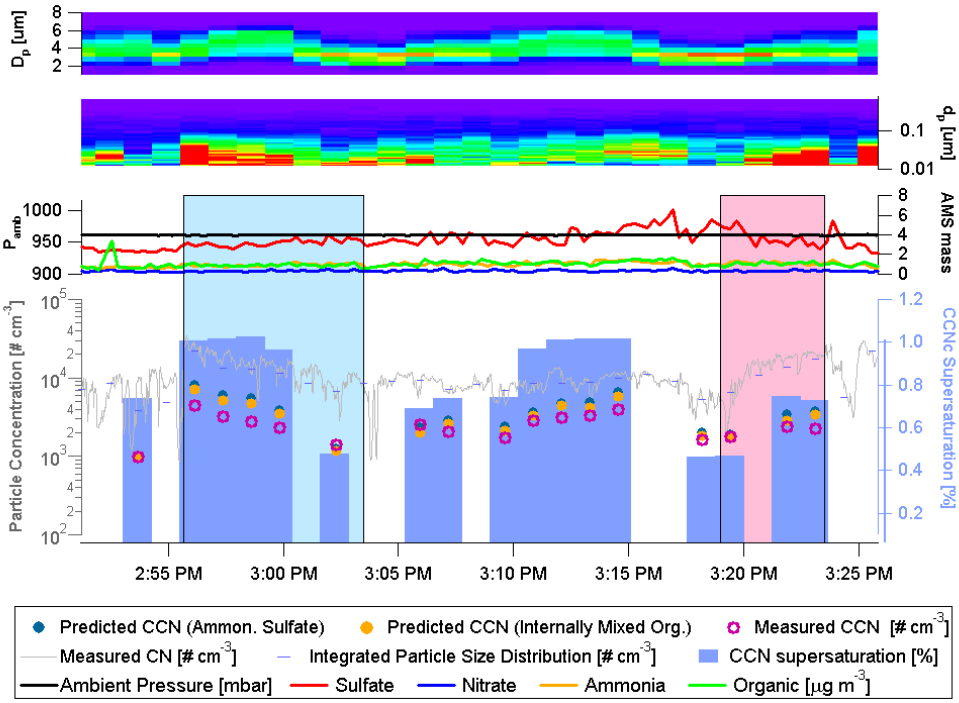
D_p [um]
d_p [um]
P_amb
AMS mass
Particle Concentration [# cm^-3]
CCNc Supersaturation [%]
2:55 PM
3:00 PM
3:05 PM
3:10 PM
3:15 PM
3:20 PM
3:25 PM
Predicted CCN (Ammon. Sulfate)
Predicted CCN (Internally Mixed Org.)
Measured CCN [# cm^-3]
Measured CN [# cm^-3]
Integrated Particle Size Distribution [# cm^-3]
CCN supersaturation [%]
Ambient Pressure [mbar]
Sulfate
Nitrate
Ammonia
Organic [μg m^-3]

(b)

1009 **Figure 8.**
1010
1011

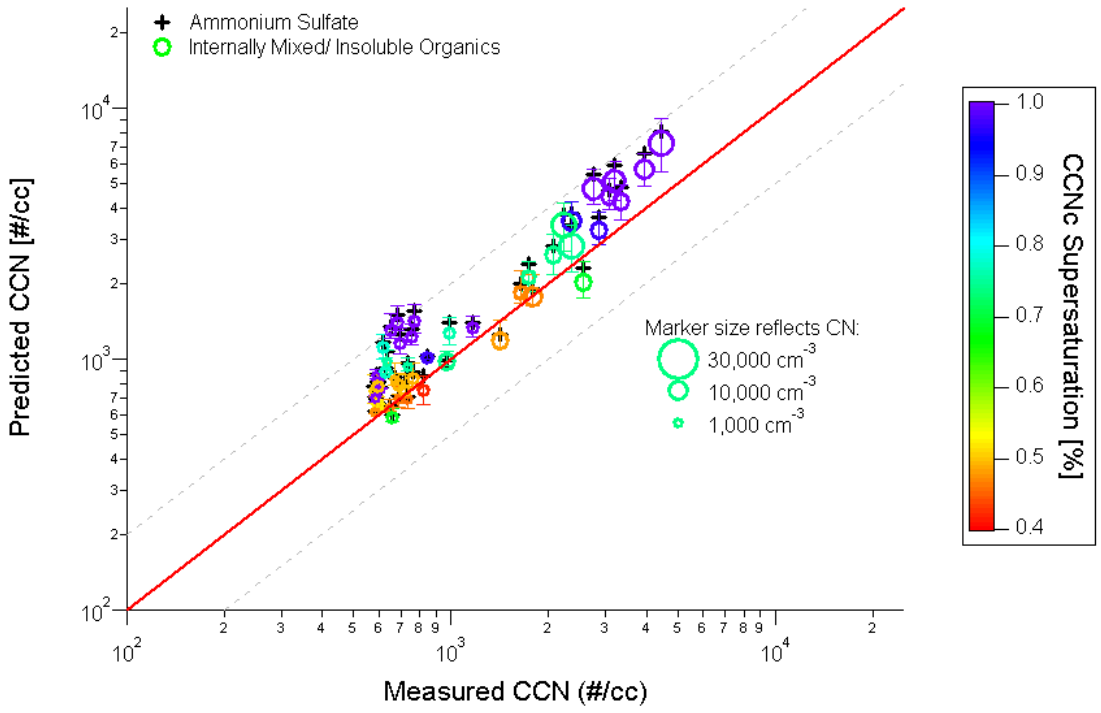

1012

1013 **Figure 9.**
1014

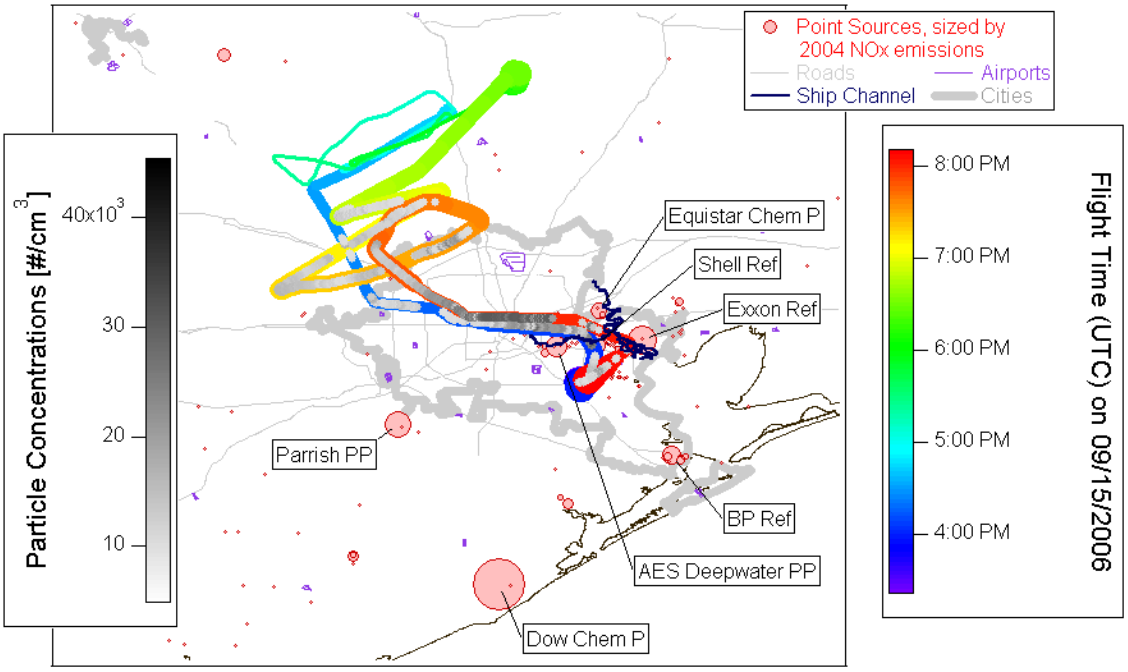

1015
1016 **(a)**
1017

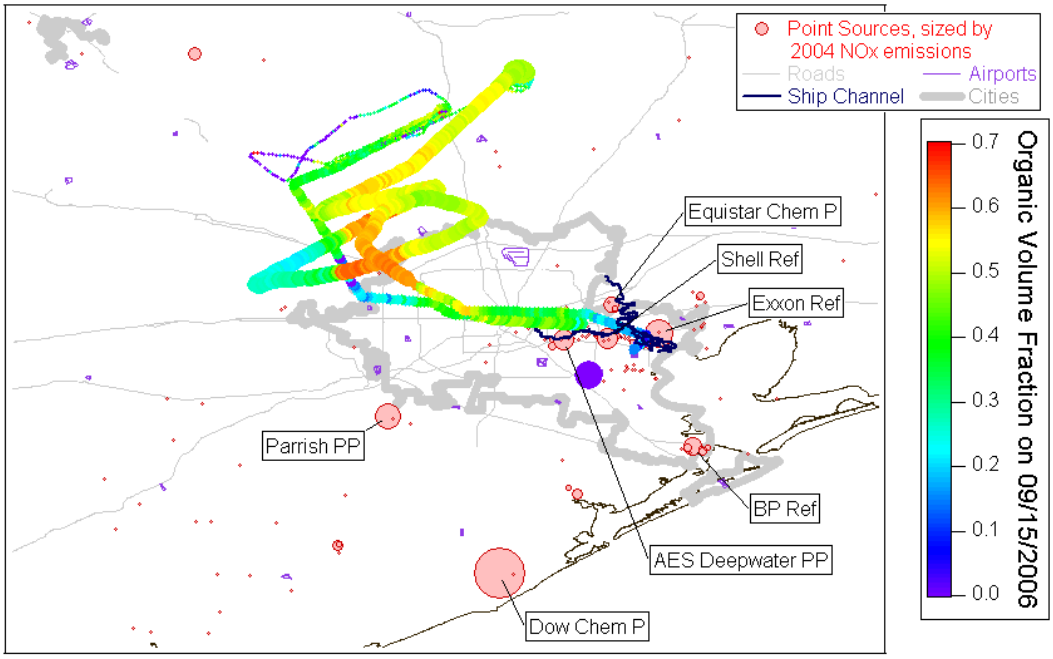

1018
1019 **(b)**
1020

1021 **Figure 10.**

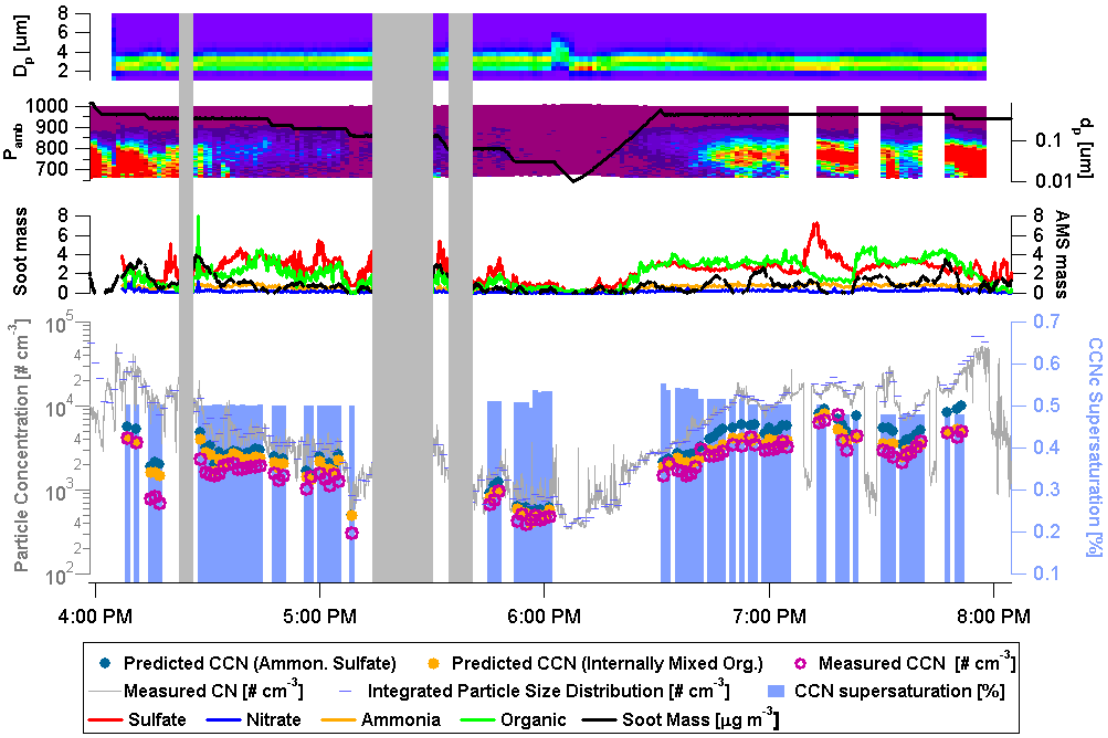

1022

1023 **Figure 11.**
1024
1025

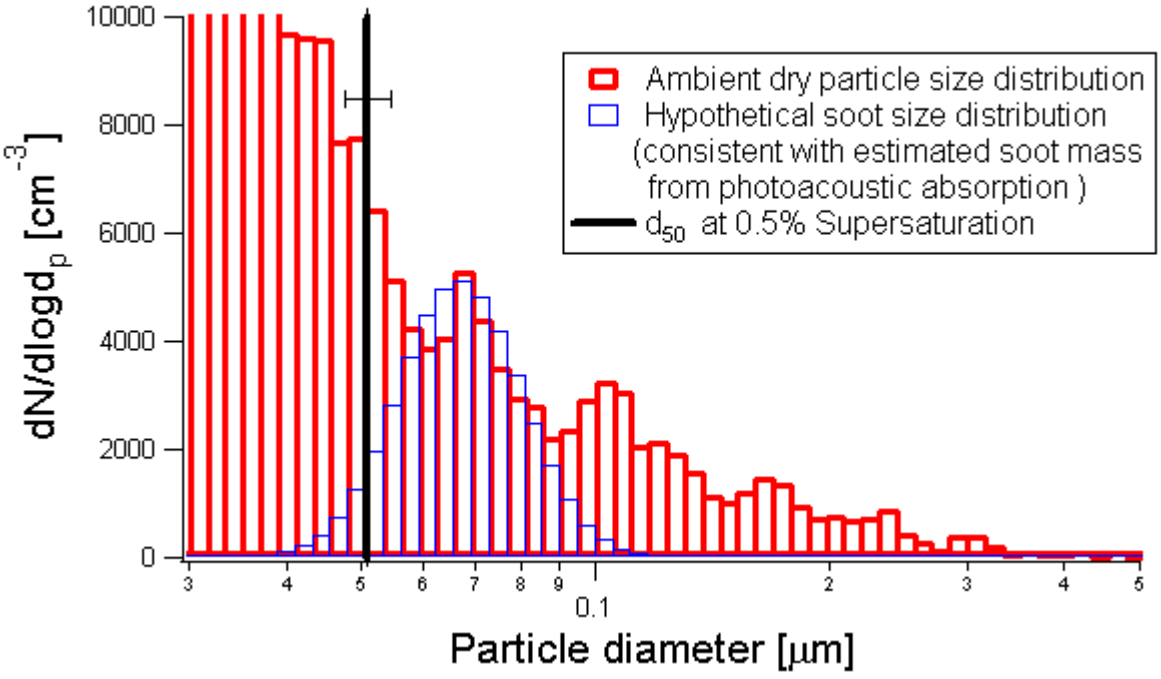

1026

1027 **Figure 12.**
1028

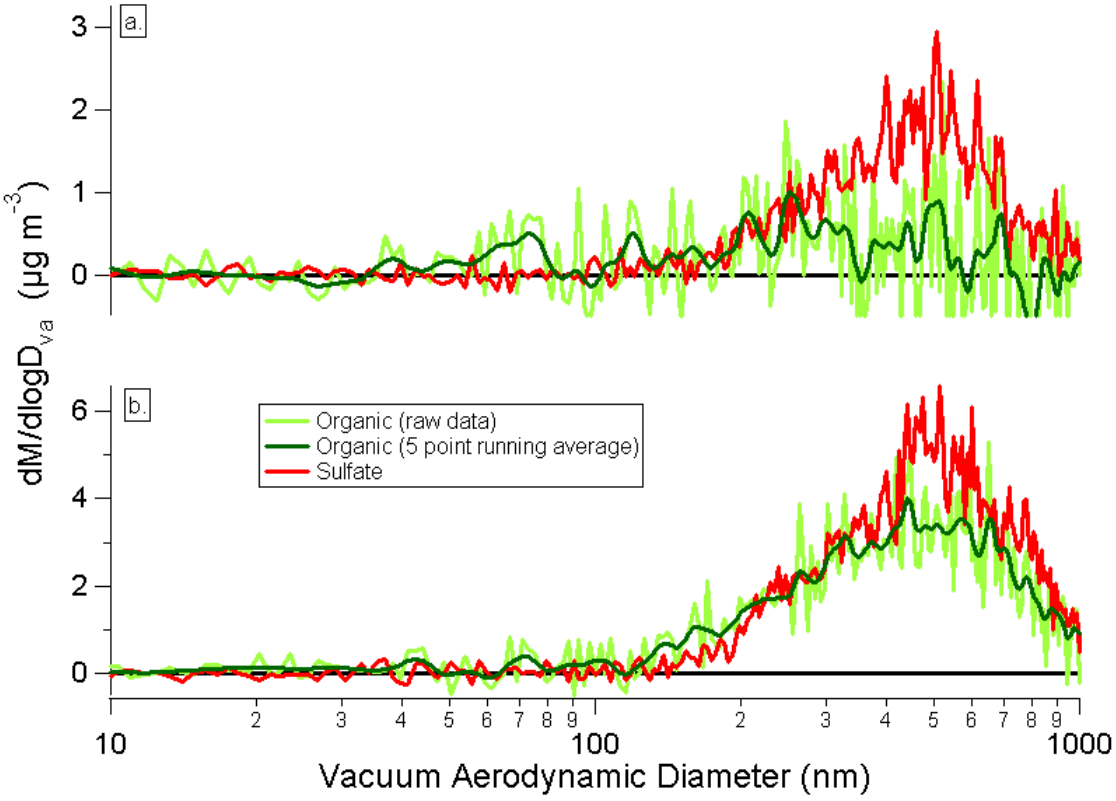

1029

Figure 13.

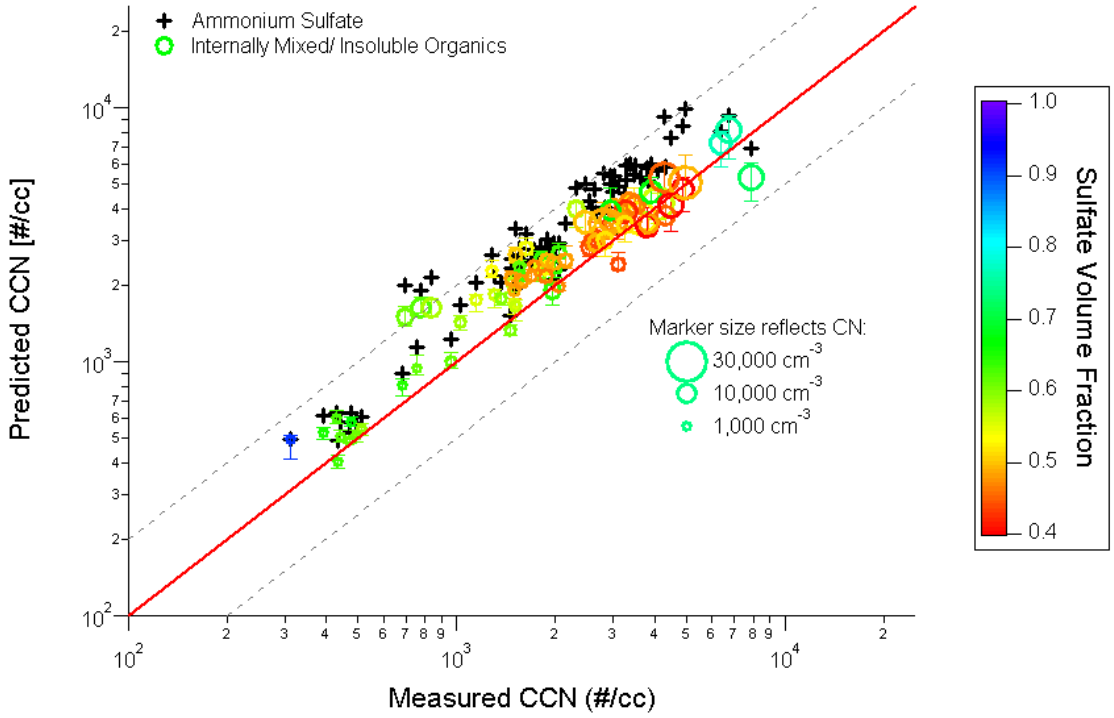
Ammonium Sulfate
Internally Mixed/ Insoluble Organics
Marker size reflects CN:
30,000 cm-3
10,000 cm-3
1,000 cm-3
Predicted CCN [#/cc]
Measured CCN (#/cc)
Sulfate Volume Fraction
1.0
0.9
0.8
0.7
0.6
0.5
0.4

1033 **Figure 14.**

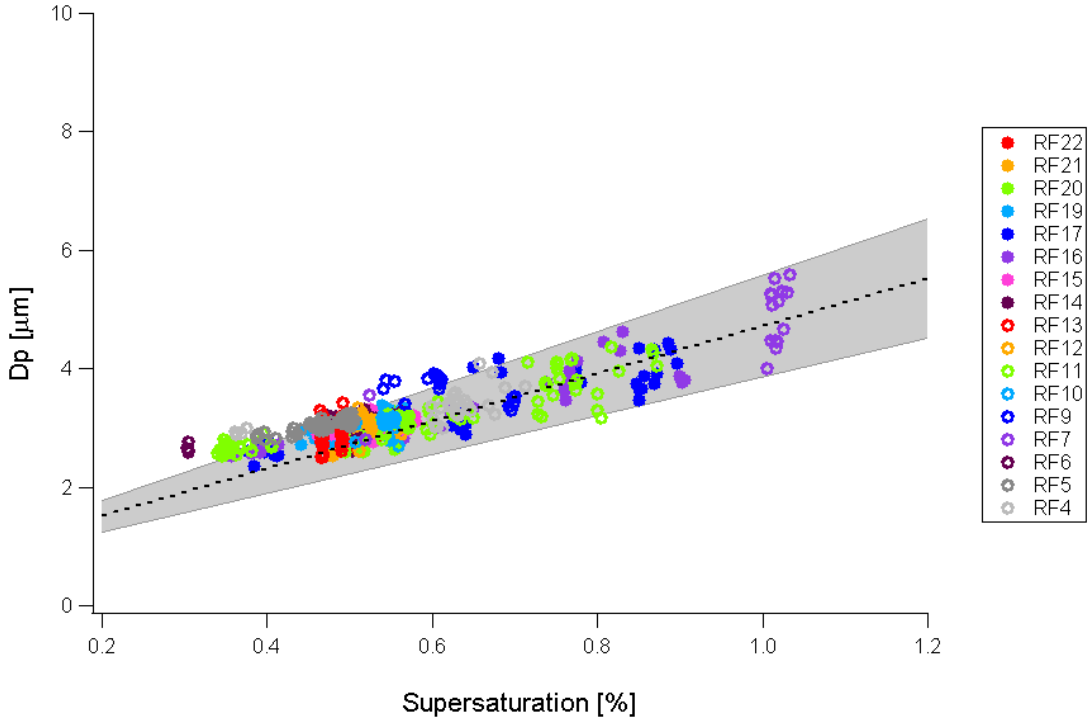

1034